JGR Solid Earth

RESEARCH ARTICLE
10.1029/2021JB023676

Rupture Model for the 29 July 2021 M_W 8.2 Chignik, Alaska Earthquake Constrained by Seismic, Geodetic, and Tsunami Observations

Lingling Ye[1], Yefei Bai[2], Daojun Si[1], Thorne Lay[3], Kwok Fai Cheung[4], and Hiroo Kanamori[5]

[1]Department of Earth and Space Sciences, Southern University of Science and Technology, Shenzhen, China, [2]Ocean College, Zhejiang University, Zhoushan, China, [3]Department of Earth and Planetary Sciences, University of California Santa Cruz, Santa Cruz, CA, USA, [4]Department of Ocean and Resources Engineering, University of Hawaii at Manoa, Honolulu, HI, USA, [5]Seismological Laboratory, California Institute of Technology, Pasadena, CA, USA

Key Points:

- The slip distribution of the 2021 Chignik M_W 8.2 earthquake is constrained by joint analysis of seismic, geodetic, and tsunami recordings
- During the ~60-s long rupture, patchy slip of up to 12.9 m occurred at depths of 32–40 km on the megathrust below the continental shelf
- The 2021 slip pattern differs from the 1938 M_W 8.2 rupture, with larger slip in the west and no slip in the easternmost 1938 rupture zone

Supporting Information:

Supporting Information may be found in the online version of this article.

Correspondence to:

L. Ye and Y. Bai,
yell@sustech.edu.cn;
yfbai@zju.edu.cn

Citation:

Ye, L., Bai, Y., Si, D., Lay, T., Cheung, K. F., & Kanamori, H. (2022). Rupture model for the 29 July 2021 M_W 8.2 Chignik, Alaska earthquake constrained by seismic, geodetic, and tsunami observations. *Journal of Geophysical Research: Solid Earth*, *127*, e2021JB023676. https://doi.org/10.1029/2021JB023676

Received 20 NOV 2021
Accepted 25 JUN 2022

Author Contributions:

Conceptualization: Lingling Ye, Thorne Lay
Formal analysis: Lingling Ye, Yefei Bai, Daojun Si, Thorne Lay, Hiroo Kanamori
Funding acquisition: Lingling Ye, Yefei Bai, Kwok Fai Cheung
Investigation: Lingling Ye, Yefei Bai, Thorne Lay, Kwok Fai Cheung
Methodology: Lingling Ye, Yefei Bai, Kwok Fai Cheung
Project Administration: Lingling Ye
Resources: Kwok Fai Cheung
Supervision: Lingling Ye, Kwok Fai Cheung, Hiroo Kanamori
Writing – original draft: Lingling Ye

Abstract A great earthquake struck the Semidi segment of the plate boundary along the Alaska Peninsula on 29 July 2021, re-rupturing part of the 1938 rupture zone. The 2021 M_W 8.2 Chignik earthquake occurred just northeast of the 22 July 2020 M_W 7.8 Simeonof earthquake, with little slip overlap. Analysis of teleseismic *P* and *SH* waves, regional Global Navigation Satellite System (GNSS) displacements, and near-field and far-field tsunami observations provides a good resolution of the 2021 rupture process. During ~60-s long faulting, the slip was nonuniformly distributed along the megathrust over depths from 32 to 40 km, with up to ~12.9-m slip in an ~170-km-long patch. The 40–45 km down-dip limit of slip is well constrained by GNSS observations along the Alaska Peninsula. Tsunami observations preclude significant slip from extending to depths <25 km, confining all coseismic slip to beneath the shallow continental shelf. Most aftershocks locate seaward of the large-slip zones, with a concentration of activity up-dip of the deeper southwestern slip zone. Some localized aftershock patches locate beneath the continental slope. The surface-wave magnitude M_S of 8.1 for the 2021 earthquake is smaller than M_S = 8.3–8.4 for the 1938 event. Seismic and tsunami data indicate that slip in 1938 was concentrated in the eastern region of its aftershock zone, extending beyond the Semidi Islands, where the 2021 event did not rupture.

Plain Language Summary The Pacific plate underthrusts the North American plate along the Alaska-Aleutian subduction zone producing great earthquakes along most of the plate boundary. The region, that ruptured in 1938, hosted another great earthquake with magnitude 8.2 on 29 July 2021 offshore of Chignik, adjacent to a magnitude 7.8 event in 2020 beneath the Shumagin Islands. Using seismic wave recordings, Global Navigation Satellite System static displacements, and tsunami wave recordings at regional and distant locations, we determine the space-time evolution of slip during the 2021 rupture process. The rupture extended northeastward ~170 km, ending just short of the Semidi Islands. The slip is concentrated on the megathrust, from 32-km to 40-km deep. Shallow slip at depths <25 km is precluded by the tsunami observations, confining all rupture to beneath the shallow continental shelf. Most aftershocks are up-dip of the large-slip regions with a concentration in the shallow region of the southwestern rupture zone. Comparisons of observations and rupture models with the 1938 event indicate distinct slip distributions and seismic energy release, with the 1938 event being somewhat larger and extending further northeast than the 2021 rupture. This provides strong evidence that the 2021 event is not a simple repeat failure of the 1938 rupture.

1. Introduction

The subduction zone along Alaska, the Alaska Peninsula, and the Aleutian Islands produces great thrust-faulting earthquakes along most of its length, as the Pacific plate underthrusts the upper North American Plate and the Bering subplate (e.g., Cross & Freymueller, 2008; Sykes, 1971; Sykes et al., 1981; von Huene et al., 2012). In the last century, great earthquakes occurred along the plate boundary in 1938 (M_W 8.2 ISC-GEM), 1946 (M_W 8.6), 1957 (M_W 8.6), 1964 (M_W 9.2), and 1965 (M_W 8.7). The 1938 rupture occurred in a region extending from the Semidi Islands southwestward to east of the Shumagin Islands, offshore of the Alaska Peninsula (Figure 1). Sykes (1971) relocated about 13 aftershocks of the 1938 event and outlined the rupture area as shown in Figure 1. The relatively long interval of 83 years since the rupture of this region, combined with geodetic measurements

Writing – review & editing: Lingling Ye, Yefei Bai, Daojun Si, Thorne Lay, Kwok Fai Cheung, Hiroo Kanamori

along the 1938 rupture zone, indicates slip deficit accumulation at a high percentage of the ~6.3 cm/yr plate convergence rate for at least the past few decades (e.g., Cross & Freymueller, 2008; Droof & Freymueller, 2021; Fletcher et al., 2001; Fournier & Freymueller, 2007; Freymueller et al., 2008; Li & Freymueller, 2018). These factors had highlighted this region, called the Semidi segment, as having high potential to rupture in a great earthquake. Indeed, this occurred on 29 July 2021, when an M_W 8.2 earthquake ruptured within the aftershock zone of the 1938 event.

The earthquake history along the Alaska Peninsula (Figure 1) appears to at least partially reflect the variation in geodetically inferred slip deficit accumulation. The high plate coupling is inferred near the Semidi Islands where a large slip was thought to have occurred during the 1938 event (e.g., Estabrook et al., 1994; Johnson & Satake, 1994). Somewhat decreased, yet still significant, coupling is inferred along the western half of the 1938 aftershock zone where some slip appears to have occurred. Only a couple of other earthquakes with magnitudes larger than 7.0 have occurred within the 1938 rupture zone prior to 2021 (Figure 1). The last great earthquake that this region previously hosted was probably in 1788 (USGS, 2013), based on tsunami deposits on Chirikof Island and further northeast on Sitkinak and Kodiak Islands along the southwestern extent of the 1964 Alaska earthquake (e.g., Briggs et al., 2014; Nelson et al., 2015). Much lower geodetic coupling of ~0.4 was measured along the Shumagin Islands prior to the 2020 event, with no resolved slip deficit measured in the southwestern portion of the Shumagin segment or along the 1946 rupture zone (e.g., Droof & Freymueller, 2021; Freymueller & Beavan, 1999). The Shumagin segment appears not to have hosted any historic earthquakes significantly larger than the 2020 event (e.g., Witter et al., 2014), with the last prior large event in its rupture zone being an M_W ~7.4 event in 1917 (e.g., Estabrook & Boyd, 1992; Davies et al., 1981; Ye et al., 2021) and only a couple of prior events larger than 7 having occurred in the down-dip region of the western Shumagin segment (Figure 1).

It is important to keep in mind that geodetic resolution of the along-dip slip deficit is very limited (Xiao et al., 2021), so the many published geodetic coupling models are not unique; most assume that coupling is a maximum (1.0) beneath the continental slope and reduces along-dip as needed to match the geodetic observations. However, it is also possible to fully match the observations with patchy down-dip locking only in the regions that have slipped in large events with known slip distributions such as the 2020 M_W 7.8 Simeonof earthquake (e.g., Bai et al., 2022; Crowell & Melgar, 2020; Elliott et al., 2022; Liu et al., 2020; Xiao et al., 2021; Ye et al., 2021). Thus, there is no current resolution of shallower strain accumulation along the Semidi or Shumagin segments on either the megathrust or on splay thrust faults in the prism (e.g., von Huene et al., 2016, 2021), making it difficult to evaluate the shallow tsunamigenic earthquake potential. The 1946 rupture (Figure 1) was one of the great tsunamigenic earthquakes of the last century, and it occurred in a region where the GPS stations on the Aleutian Islands are also essentially blind to any recent near-trench strain accumulation. The rupture extent for the 1938 event suggested by the aftershock region (Figure 1) is also very unlikely to correspond to the region of large coseismic slip (or of any subsequent slip deficit accumulation) as the aftershock locations are quite poorly resolved (e.g., Boyd & Lerner-Lam, 1988), and it is very common to observe aftershocks well outside of large-slip regions for megathrust earthquakes (e.g., Wetzler et al., 2018).

The importance of establishing the slip distribution of large megathrust earthquakes for understanding the overall strain accumulation and frictional behavior of the plate boundary motivates this study, in which seismic, geodetic, and tsunami observations are combined to constrain the space-time slip history during the 2021 M_W 8.2 Chignik earthquake. The resulting well-resolved slip model is then compared to available data and slip characterizations for the 1938 M_W 8.2 earthquake to assess the degree of similarity of the repeated rupture of the Semidi segment. The analysis addresses whether shallow slip occurred on the megathrust coseismically in the 2021 event, which is relevant to the important question of whether the up-dip portion of the plate boundary has accumulated strain and is capable of a 1946-type strongly tsunamigenic failure (e.g., Kanamori, 1972; Okal & Hébert, 2007).

2. Data and Methods

2.1. Point-Source Information

The great 29 July 2021 Chignik, Alaska earthquake began at 06:15:49.2 UTC with an estimated hypocentral location at 55.364°N, 157.888°W, 35.0-km deep [US Geological Survey-National Earthquake Information Center (USGS-NEIC): https://earthquake.usgs.gov/earthquakes/eventpage/ak0219neiszm/origin/detail]. Long-period point-source moment tensor solutions indicate a shallowly dipping thrust focal mechanism which is consistent

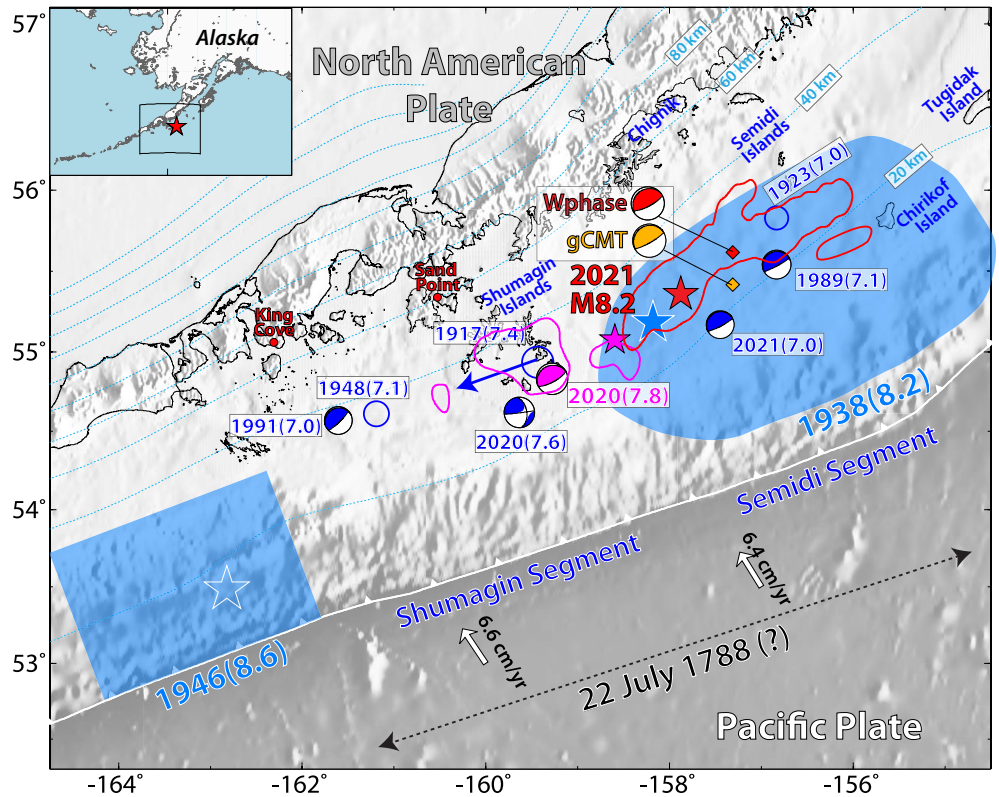

Figure 1. Source regions of the 29 July 2021 M_W 8.2 Chignik, Alaska earthquake (slip >2 m from our preferred model outlined in red, with the red star indicating the USGS-NEIC epicenter) and the 22 July 2020 M_W 7.8 Simeonof earthquake (Ye et al., 2021; slip >1.0 m outlined in magenta, with magenta star indicating the USGS-NEIC epicenter). Our *W*-phase focal mechanism for the 2021 Chignik earthquake is shown along with a red diamond locating its centroid position. The blue shaded regions indicate aftershock zones of the 1946 M_W 8.6 and 1938 M_W 8.2 earthquakes with the USGS-NEIC epicenters shown by large white stars. Labeled blue circles and focal mechanisms (with radius scaled by magnitude) indicate the USGS-NEIC epicenters for regional event with $M_W \geq 7.0$ since 1900. The 20-km depth intervals along the plate boundary interface model of Slab2 (Hayes et al., 2018) are indicated by cyan thin dashed lines. Plate convergence direction and rate of the Pacific plate relative to a fixed North America plate are shown by white arrows for the MORVEL model of DeMets et al. (2010). The uncertain rupture extent of the historic 1788 event is indicated. King Cove and Sand Point are locations of tidal gauge stations used in the tsunami analysis.

with rupture on the plate boundary megathrust. The USGS *W*-phase moment tensor has a seismic moment, $M_0 = 2.36 \times 10^{21}$ N m (M_{WW} 8.18), and a 35.5 km centroid depth. The moment tensor is pure double couple with strike, $\phi = 239°$, dip, $\delta = 14°$, and rake, $\lambda = 95°$. The quick global Centroid Moment Tensor (gCMT) solution has $M_0 = 2.96 \times 10^{21}$ N m (M_W 8.2), 30.2 km centroid depth, 32.8 s centroid time shift, and best double couple $\phi = 236°$, $\delta = 10°$, $\lambda = 86°$ (https://www.globalcmt.org/CMTsearch.html). We perform a *W*-phase moment tensor inversion (Kanamori & Rivera, 2008) using 274 channels of ground motion recordings in the passband 0.002–0.005 Hz from 104 global broadband seismic stations, obtaining a solution with $M_0 = 2.06 \times 10^{21}$ N m (M_W 8.14), 40.5 km centroid depth, and 33 s centroid time, with $\phi = 233.2°$, $\delta = 15.2°$, $\lambda = 81.5°$, at the centroid location (55.62°N, 157.32°W; Figure 1). The fault plane orientation from this solution provides a starting geometry for the subsequent finite-fault inversions. The centroid location is consistent with primarily northeastward expansion of the rupture from the USGS hypocenter mapped by the red star in Figure 1.

2.2. Seismic, Geodetic, and Tsunami Data

We include seismic, geodetic, and tsunami observations to resolve the space-time history of rupture (Figure 2). The seismological data set involves teleseismic *P* and *SH* ground displacement recordings from global broadband stations, downloaded from the Incorporated Research Institutions for Seismology (IRIS; https://iris.edu/hq/). We use 107 vertical component *P* waves and 43 horizontal component *SH* waves filtered in the passband 0.005–0.9 Hz

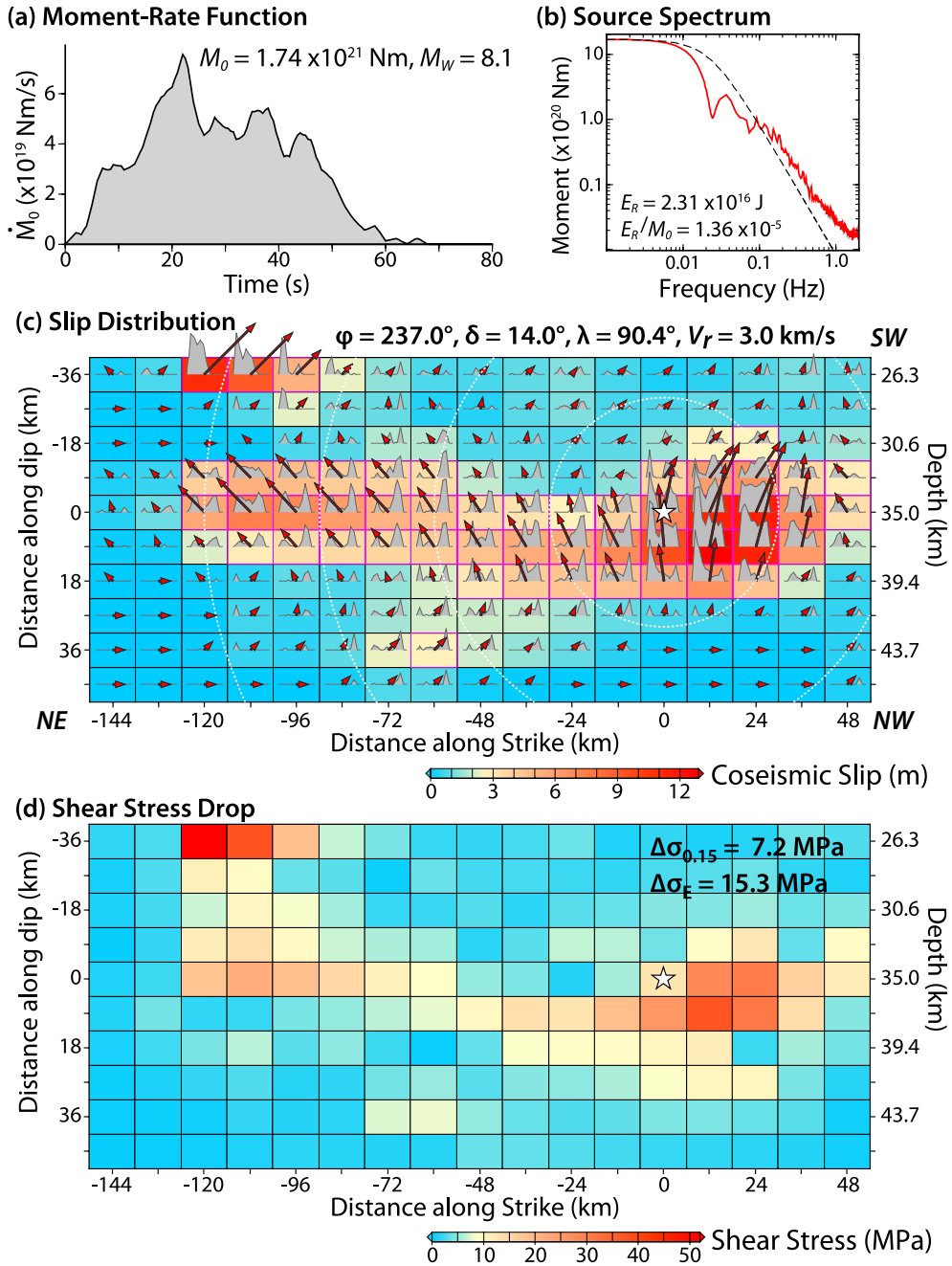

Figure 2. Preferred rupture model for the 2021 Chignik, Alaska earthquake obtained by iterative inversion of seismic and geodetic observations and forward modeling of tsunami observations. (a) Moment-rate function (MRF) with total seismic moment M_0 and corresponding M_W. The centroid time is 28.2 s, and the source duration is ~60 s. (b) Far-field source spectrum (red curve) determined from the MRF for periods <20 s and from stacks of propagation-corrected broadband *P* wave spectra for periods from 20 to 0.5 s. The dashed curve is an ω^{-2} spectrum with 3 MPa stress drop and equal M_0 for reference. (c) Slip distribution on the fault with strike, $\phi = 237°$, dip $\delta = 14°$, and average rake, $\lambda = 90.4°$, with the slip magnitude and direction shown by arrows and colors for each subfault. The subfault source time functions are shown as polygons in each subfault. The maximum rupture expansion speed is specified as 3.0 km/s with the dashed white curves indicating the rupture expansion front in 10-s intervals. (d) Shear stress change calculated from the slip distribution in (c) for a half space (Okada, 1985; Ye, Lay, et al., 2016). Data fits for this model are shown in Figures 3 (seismic), 4 (geodetic), and 7 (tsunami).

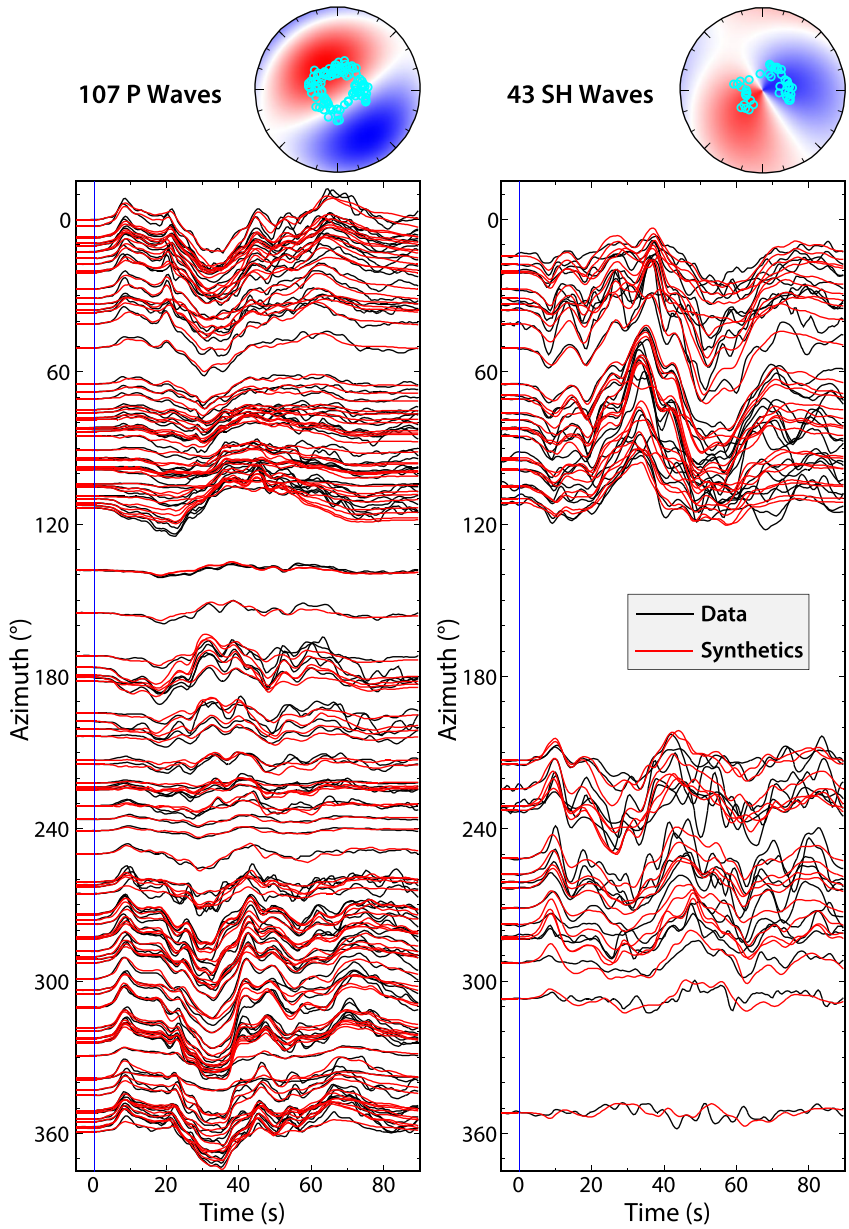

Figure 3. Waveform fits of teleseismic broadband ground displacement *P* waves (left) and *SH* waves (right) for the 2021 Chignik earthquake. Observed waveforms are shown by black traces and predictions for our preferred model (Figure 2) by red traces, with relative amplitudes. The lower hemisphere stereographic projections at the top show the azimuths and take-off angles of the data and the radiation patterns (red for compressional *P* motion and clockwise *SH* motion).

in the analysis (Figure 3). The geodetic data are from regional Global Navigation Satellite System (GNSS) stations, where the three-component coseismic static ground displacements were obtained from UNAVCO (https://unavco.org; Blewitt et al., 2018), with the station locations shown in Figure 4. The tsunami data include tide gauge recordings from nearby stations King Cove and Sand Point along the Alaska Peninsula and Alitak on Kodiak Island, as well as seafloor pressure sensor recordings from the NOAA Deep-ocean Assessment and Reporting of Tsunamis (DART) buoys (https://www.ndbc.noaa.gov/obs.shtml?lat=13%26lon=-173%26zoom=2%26pgm=tsunami), and tide gauge recordings from Hilo and Kahului in Hawaii, with the station locations shown in Figure 5. The combined data set provides good resolution of the slip distribution through finite-fault inversion of seismic and geodetic data and forward modeling of tsunami records.

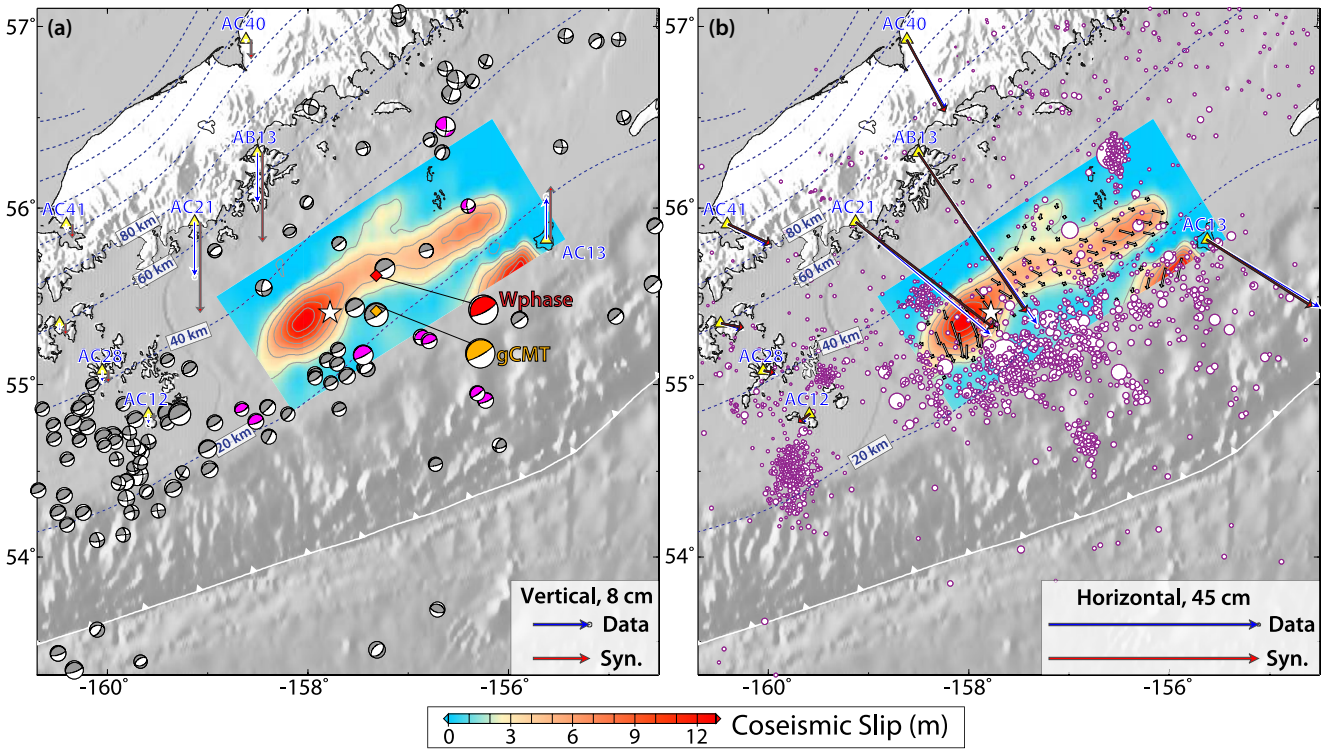

Figure 4. Map views of the 2021 Chignik slip model (Figure 2) with the fitting to the closest static Global Navigation Satellite System (GNSS) data. (a) The slip model along with all global Centroid Moment Tensor (gCMT) focal mechanisms for historical events from 1976 to 2021 (gray) and aftershocks (pink). The white star indicates the epicenter used in the slip inversion (Lat 55.41°N, Lon 157.78°W). The gCMT and W-phase mechanisms for the 2021 mainshock are shown with tie lines to their respective centroid locations. Blue and red vectors show comparisons of observed vertical coseismic displacements and model predictions at GNSS stations, respectively. The largest observed vertical displacement is about 8 cm at station AB13. (b) The same slip model is shown with regional seismicity from the USGS-NEIC catalog with $M > 2.5$ within 4 months after the 2021 M_W 8.2 event (circles with radius scaled by magnitude). Note that aftershocks of the Chignik earthquake are primarily located up-dip of the coseismic large-slip zone, including the largest event, the 14 August 2021 M_W 6.9 event up-dip of the hypocenter. Blue and red vectors show comparisons of observed horizontal coseismic displacements and model predictions at GNSS stations. The largest observed horizontal displacement is about 45 cm at station AB13. The root-mean-square misfit is 3.56 cm.

2.3. Finite-Fault Inversion Method

We jointly invert the teleseismic *P* and *SH* data and the regional GNSS static displacement measurements using a least-squares kinematic finite-fault inversion procedure based on Hartzell and Heaton (1983), Kikuchi and Kanamori (1991), and Ye, Lay, et al. (2016). Guided by our *W*-phase inversion we initially considered planar-fault models with $\phi = 233.2°$ and $\delta = 15.2°$, allowing rake to vary within each subfault. The source time functions for each subfault are parameterized by overlapping triangular time functions that provide flexibility in the specific time history for each subfault slip. The earliest allowed rupture onset of each subfault is determined by expanding circular isochrones with a designated rupture velocity. We performed preliminary inversions and tsunami modeling assuming the plate boundary interface geometry given by the Slab2 model (Hayes et al., 2018). However, the multichannel seismic (MCS) survey of ALEUT 3 (Kuehn, 2019) suggests that the plate interface in the Semidi segment is systematically deeper than that in the Slab2 model (Hayes et al., 2018) by about 2–6 km, and this is more consistent with the final hypocenter depth of 35.0 km from the USGS-NEIC (Figure S1 in Supporting Information S1). Thus, we shifted the fault plane of the slab megathrust by about 6.5-km deeper, although there are at least a few kilometers of depth uncertainty, as indicated by the spread of reflections in the ALEUT 3 MCS survey. In our preferred slip model, we adopt a dip angle of 14° from the slab geometry as indicated by both the Slab2 model and the ALEUT 3 MCS survey (Figure S1 in Supporting Information S1).

2.4. Iterative Inversion and Modeling Strategy

Having constrained the fault model geometry to reflect the long-period seismic wave mechanism and the plate interface dip and depth from the ALEUT 3 MCS survey, there are still many poorly constrained parameters in

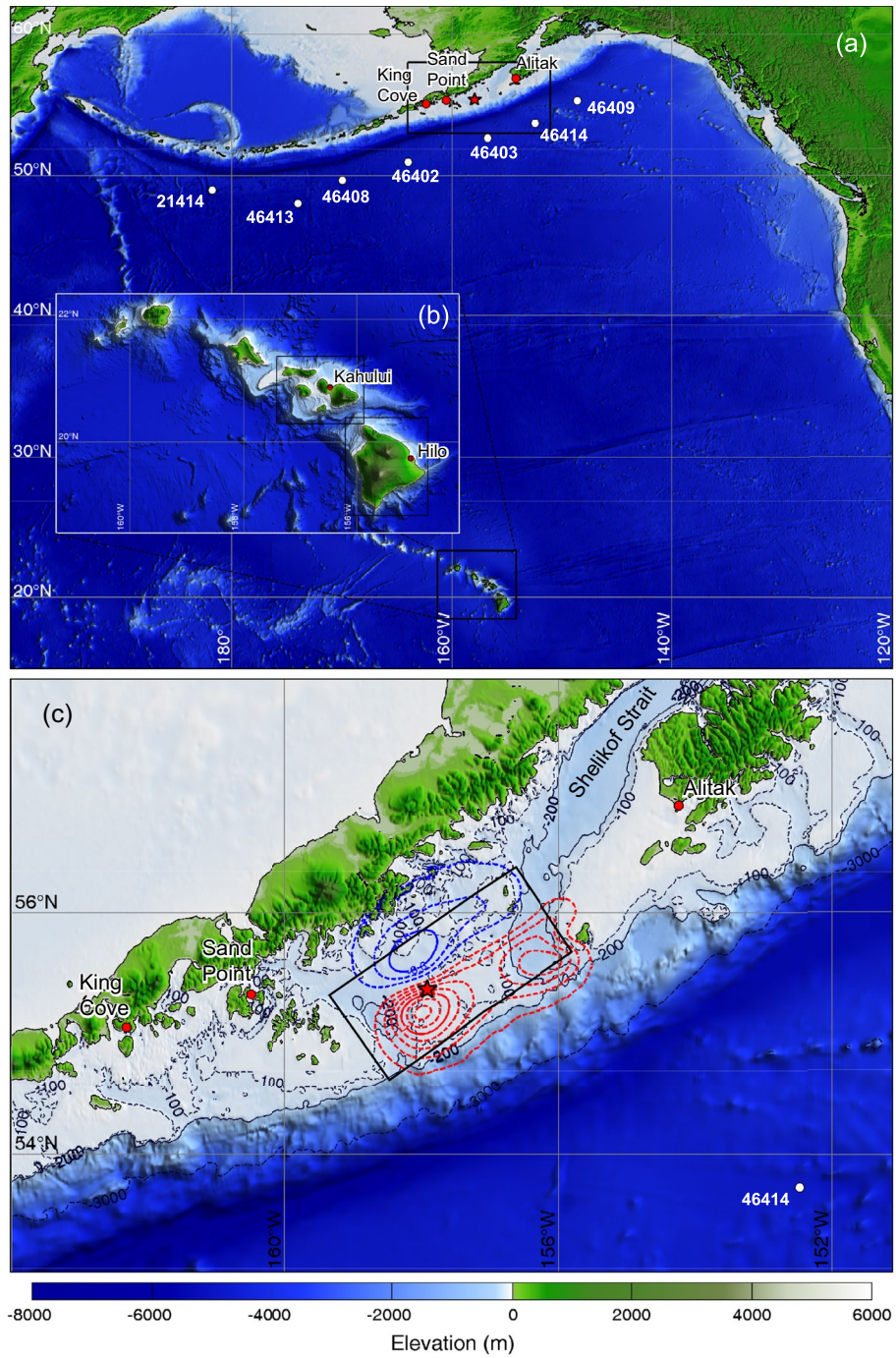

Figure 5. Computational grids, digital elevation models, coseismic seafloor deformation, and location maps. (a) Level-1 grid with outlines of level-2 grids denoted by rectangles. (b) Level-2 Hawaii grid with outlines of level-3 grids indicated by rectangles. (c) Level-2 Alaska grid with the fault model from Figure 2 delineated by black rectangle, uplift and subsidence indicated by red and blue contours at 0.2-m intervals, and 100-m, 200-m, and 3,000-m water depth contours denoted by dashed lines. Red star denotes the epicenter, and white and red circles, respectively, indicate locations of DART and tide gauge observations used in forward modeling. Our finite-fault model is confined landward of the continental shelf break which is near the 200-m water depth contours.

finite-fault inversions, including the dimensions of the fault model, the kinematic constraints on the rupture timing controlled by rupture velocity and the subfault source time functions, and the absolute placement of the hypocenter on the fault model. Some bounds on these parameters are provided by the joint inversion of seismic and geodetic data, with the GNSS static displacement data providing particularly important information on the

down-dip and along-strike extent of slip given the station distribution (Figure 4). However, the joint inversions provide very little reliable constraint on the up-dip extent of the rupture and only secondary information on the absolute fault placement. Previous work has demonstrated the advantage of using tsunami recordings seaward of the rupture along with landward tide gauge or runup observations, to iteratively adjust the fault dimensions along-dip and along-strike, as well as the absolute placement of the fault model and the kinematic parameters affecting the inverted slip distribution (e.g., Bai et al., 2014; Heidarzadeh et al., 2016; Li et al., 2016; Yamazaki, Lay, et al., 2011, 2013; Ye, Kanamori, et al., 2016; Yue et al., 2014). An iterative process of joint inversion of the seismic and geodetic data, prediction of the tsunami signals, and adjustment of the fault model parameters is applied rather than direct joint inversion of all data (e.g., Romano et al., 2020; Yokota et al., 2011), due to the nonlinear perturbations arising from modifying the fault grid, computing the tsunami excitation and correcting for tsunami arrival time shifts. For this event, the primary perturbations to our starting model (Figure S2 in Supporting Information S1) involve the reduction of the up-dip extent of the model as required to fit the tsunami observations. Similar reductions are needed for the seismo-geodetic inversion model of Liu et al. (2022) (Figure S3 in Supporting Information S1). We first summarize the final result and then discuss how it was arrived at.

3. Results and Discussion

3.1. Seismo-Geodetic Final Slip Model

Our preferred model for the 29 July 2021 Chignik mainshock (Figure 2) is obtained by the iterative inversion and forward modeling procedure. The model grid has 17 12 km × 9 km subfaults along-strike and 10 along-dip. The faulting geometry has strike $\phi = 237°$ and dip $\delta = 14°$ with the average rake $\lambda = 90°$ and seismic moment $M_0 = 1.74 \times 10^{21}$ N m ($M_W = 8.1$). The centroid time of the moment-rate function (MRF) is 28.2 s and the centroid depth of the slip distribution is 34.9 km. These overall parameters are very similar to the long-period point-source inversions, so the model is compatible with long-period seismic motions. In the course of the iterative modeling, the earthquake epicenter was slightly shifted to a final position at 55.41°N, 157.78°W. The subfault source time functions are parameterized with 9 2-s rise-time triangles with eight 2-s offsets, giving possible total subfault durations of 20 s. In our preferred slip model, large-slip subfaults around the hypocenter typically have durations of ∼20 s, whereas shallower and easterly subfaults typically have 10–12-s duration or long jagged source time functions (Figure 2c). The slip distribution is dominated by a large-slip patch extending northeastward by ∼170-km along-strike, at depths from ∼32 to ∼40 km centered below the hypocenter, with slip diminishing ∼50 km northeast from the epicenter (Figure 4). The peak slip is ∼12.9 m, with a substantial area having >7 m of slip (Figure 2c). Peak slip is not a stable feature of finite-fault inversions, as it varies with model parameterization and smoothing (Figure S4 in Supporting Information S1). The up-dip extent of rupture is constrained to ∼25-km depth primarily by the tsunami data. The down-dip extent of the rupture, ranging from 40 to 45 km (in a localized patch), is constrained primarily by the GNSS observations along the Alaska Peninsula, with coseismic displacements in the Shumagin Islands and Chirikof Island and the tsunami observations constraining the along-strike extent of the slip zone. There is moderate variability of rake in the slip distribution, with some average difference between the two main patches separated by the seaward shift of slip consistently found in various models through the iterative process. Neglected along-strike curvature of the actual megathrust may have some trade-off with the rake variations. The slip in the shallowest row of the model at the far edge from the hypocenter is variable between models. This feature is a result of late weak energy in the *P* and *SH* waves and is not reliably resolved. In addition, a localized slip patch with ∼3-m slip at depths from 40 to 45 km extends down-dip from the northeastern large-slip patch.

The rupture duration is well resolved to be ∼60 s, with minor poorly resolved moment rate continuing out to 70 s. The source spectrum (Figure 2b), obtained from the MRF for periods <20 s and from stacked broadband *P* wave spectra corrected for propagation effects for shorter periods (e.g., Ye, Lay, et al., 2016), is moderately enhanced in short-period energy and has a radiated energy estimate of $E_R = 2.31 \times 10^{16}$ J, with a moment-scaled value of 1.36×10^{-5}. This value is comparable to the 3.1×10^{16} J broadband radiated energy estimate routinely computed by IRIS (http://ds.iris.edu/spud/eqenergy/19194587) using the method of Convers and Newman (2011). The moment-scaled value is somewhat higher than the average found for large interplate thrust ruptures (1.06×10^{-5}) by Ye, Lay, et al. (2016). The spectrum has a deep notch at ∼50-s period and deviates significantly from a simple ω^{-2} spectrum with the same seismic moment and a 3 MPa stress drop. The shear stress change on the fault is

shown in Figure 2d, and two procedures are used to estimate the static stress drop. One estimate uses the cumulative area and moment of subfaults with moment ≥15% of the peak subfault moment in a circular crack model, giving $\Delta\sigma_{0.15} = 7.2$ MPa. The second estimate is a slip-weighted estimate using the actual slip distribution, giving $\Delta\sigma_E = 15.3$ MPa. These estimates are obtained using the procedure described in Ye, Lay, et al. (2016), and are somewhat higher than the average value for large interplate thrust events (~3.4–4.6 MPa). Given the dependence of slip values on the model parameterization, there is uncertainty at least a factor of 2 in the stress drop measures, as is the case for all events (Ye, Lay, et al., 2016).

The final slip model is shown in the map view in Figure 4 along with observed and predicted GNSS coseismic static displacements. Most of the slip zone is confined between the 20-km and 40-km depth contours of Slab2, with slip extending somewhat shallower in the eastern end of the model. The matching of arrival times and wave amplitudes at DART stations plays a major role in delimiting the model, as does the displacement at GNSS station AC13 just beyond the southeast edge of the model. The static GNSS displacements are generally well fit (the RMS misfit is 3.56 cm; Table S1 in Supporting Information S1), particularly the horizontal motions, with the nearby vertical motions along the Alaska Peninsula being somewhat overpredicted. This may be influenced by the dip of the down-dip edge of the planar model, which has some uncertainty.

The observed teleseismic *P* and *SH* waveforms and final model synthetics are shown in Figure 3. The azimuthally distributed waveforms are well fit for the most part, through about 80 s of the signals, although the *SH* waves do have intermittent features that are not accounted for by the model and may correspond to unmodeled *ScS* or receiver scattered energy. The model accounts for about 86% of the power in the observed signals, which is a good fit for least-squares joint inversions of teleseismic and geodetic data. Comparably good fits to seismic and geodetic observations were obtained for initial inversions (such as the one shown in Figure S2 in Supporting Information S1) using model grids that extended further along-strike and along-dip, prior to the iterative modeling of tsunami observations that adjusted the fault model extent, kinematic parameters and hypocenter to the final version shown here. Very little compromise in the fitting of the seismic and geodetic data occurred with the adjustments, but the improvement in fit to the tsunami signals was pronounced relative to initial models that extended slip to shallower depth.

3.2. Tsunami Modeling

The 2021 earthquake generated a tsunami with clear signals at DART stations seaward of the Aleutian trench, as well as regional tide gauges to the east and west of the source that we use to constrain the seismo-geodetic inversion through forward tsunami modeling (see Figure 5 for location maps). Two Hawaii tide gauges also recorded distinct tsunami signals and their sensitivity to incident wave periods provides an additional constraint in evaluation and selection of the final model. NEOWAVE has been a proven tool for this iterative inversion and forward computation. The depth-integrated nonhydrostatic model utilizes a vertical velocity term to describe tsunami generation from seafloor deformation, wavenumber dependent shoaling and deshoaling on sloping seafloors, and dispersion of short-period waves during propagation (e.g., Bai et al., 2018; Yamazaki et al., 2009; Yamazaki, Cheung, et al., 2011), which are important attributes in accurate reproduction of the DART and tide gauge records for convergence of the final source model (e.g., Bai et al., 2014; Li et al., 2016; Yamazaki et al., 2013, 2018; Ye, Kanamori, et al., 2016).

NEOWAVE utilizes a system of nested computational grids to describe multiscale tsunami processes from the open ocean to the shore with increasing resolution. Figure 5a shows the coverage of the level-1 grid extending from Alaska to Hawaii and California. The 2-arcmin grid describes wave propagation over large-scale bathymetric features and reflection from land masses with optimal dispersion properties (Li & Cheung, 2019). The level-2 grid in Figure 5c resolves the near-field wave processes at 0.5 arcmin over the continental shelf along the Alaska Peninsula for computation of tide gauge signals. Figure 5b shows a second level-2 grid at 0.4 arcmin around the Hawaiian Islands as well as arrangement of level-3 grids at 0.6 arcsec. Tsunami signals at the Kahului and Hilo tide gauges are computed within level-4 grids of 0.3 arcsec (~9 m) which is needed to resolve the nearshore reef systems and breakwaters. The four levels of nested grids are coupled with two-way hierarchical communications among computations of different resolutions. The subgrid roughness, which becomes a factor in shelf hydraulic processes, is described by a Manning's coefficient of 0.025. The 0.5-arcmin GEBCO data set provides the background digital elevation model, which is augmented by high-resolution NCEI data sets for the Alaska Peninsula as well as LiDAR and multibeam data of 1–50-m resolution in Hawaii waters.

Implementation of a source model with the planar-fault solution of Okada (1985) provides the time history of seafloor deformation. The vertical displacement, which is augmented by horizontal movement of the local seafloor slope following the method of Tanioka and Satake (1996), defines the boundary conditions for tsunami modeling. This correction has minor effects over the relatively flat continental shelf, but becomes important beyond the shelf break at ~200-m water depth. The final source model produces moderate subsidence landward of the epicenter and an elongated uplift patch with two distinct peaks reaching ~1.5-m seaward of the large-slip zone (Figure 5c). The location of the primary seafloor deformation over the continental shelf plays a crucial role in the resulting tsunami. Movie S1 shows trapping of long-period tsunami waves over the shallow shelf as well as immediate onshore and offshore propagation of shorter waves generated by minor uplift extending onto the continental slope. The colocation of the northeastern uplift peak and the Shelikof Strait outlet enhances offshore propagation of the initial tsunami wave as well as leakage of trapped waves from the shelf. Movie S2 depicts persistent long-period oscillations over the Alaska-Aleutian shelf and propagation of leaked waves across the North Pacific Ocean.

The computation covers an elapsed time of 10 hr to capture local amplification from constructive interference of wave components over continental and insular shelves. Figure 6 provides the amplitude plots to demonstrate the near-field and far-field wave patterns from the final model. The wave amplitude reaches 1.4 m near the epicenter, but rapidly decreases to 0.05 m at the nearest DART 46403 due to energy trapping by the shelf and wave deshoaling over the continental slope. A radiation pattern originating from the Shelikof Strait outlet is evident across the Northeast Pacific Ocean. The main energy lobe extending toward Northern California generates standing edge waves over the continental shelf, corroborating the ~60-min oscillations observed at the North Spit tide gauge for over 24 hr (https://tidesandcurrents.noaa.gov/). The sidelobe waves approaching Hawaii reduce to ~1-cm amplitude, before being shoaled and amplified to 0.1 m over the interconnected insular shelves prone to resonance oscillations (Cheung et al., 2013).

The computed and recorded tsunami signals show good overall agreement at the tide gauge stations (Figure 7), indicating reproduction of the dominant seafloor deformation pattern by the final model. The westernmost DART 21414 registers a multibanded signal with the highest peak at ~90-min period associated with the along-strike dimension of the uplift patch. A ~60-min component from the along-dip uplift becomes more evident toward the east and constitutes the primary signal at DART 46403 nearest to the epicenter, where the ~90-min component reduces to the lowest level before re-emerging at the two stations further east. The leakage of trapped waves from the shelf generates small amplitude, but persistent long-period oscillations. The slight extension of the uplift patch beyond the shelf edge and the location of the uplift peaks in deeper water over the shelf results in shorter period waves with ~30–40-min period in both the onshore and offshore directions. The tide gauge signals corroborate the DART records with the ~100-min dominant component at King Cove and Alitak to the east and west of the rupture, and a more even distribution of the various components at Sand Point to the northwest. The Hilo and Kahului tide gauges register both the ~30–40-min and ~60-min components, but the background oscillations induced by swells and wind waves might have caused the phase shift between the computed and recorded time series.

3.3. Comparison With Other Finite-Fault Solutions

The USGS computed two finite-fault solutions for the 2021 Chignik earthquake (https://earthquake.usgs.gov/earthquakes/eventpage/ak0219neiszm/finite-fault), neither being constrained by tsunami modeling. A standard inversion with only teleseismic body waves and surface waves, for a planar-fault model with $\phi = 243°$ and $\delta = 14°$ yielded $M_0 = 2.88 \times 10^{21}$ N m (M_W 8.24), with a 100-s long duration, and peak slip of 2.9 m. An inversion for the same fault orientation using the same seismic waves plus 1 strong motion recording, 6-hr-GNSS time series, and 16 static GNSS observations yielded $M_0 = 2.89 \times 10^{21}$ N m (M_W 8.24), with ~70-s duration and peak slip 4.8 m. Liu et al. (2022) jointly inverted regional and teleseismic data along with coseismic static and hr-GNSS displacements for a slip model extending ~175 km northeastward with peak slip of ~8.6 m in the depth range of 20–40 km (Figure S3 in Supporting Information S1). These models have somewhat deeper slip in near the hypocenter, and a distribution of slip along-strike that shifts to shallower depths to the northeast as in our preferred model (Figures 2 and 3). The slip in these models also stops short of the Semidi Islands (the second USGS model does not use GNSS from those islands). Due to having further slip that extends up-dip to near the continental shelf

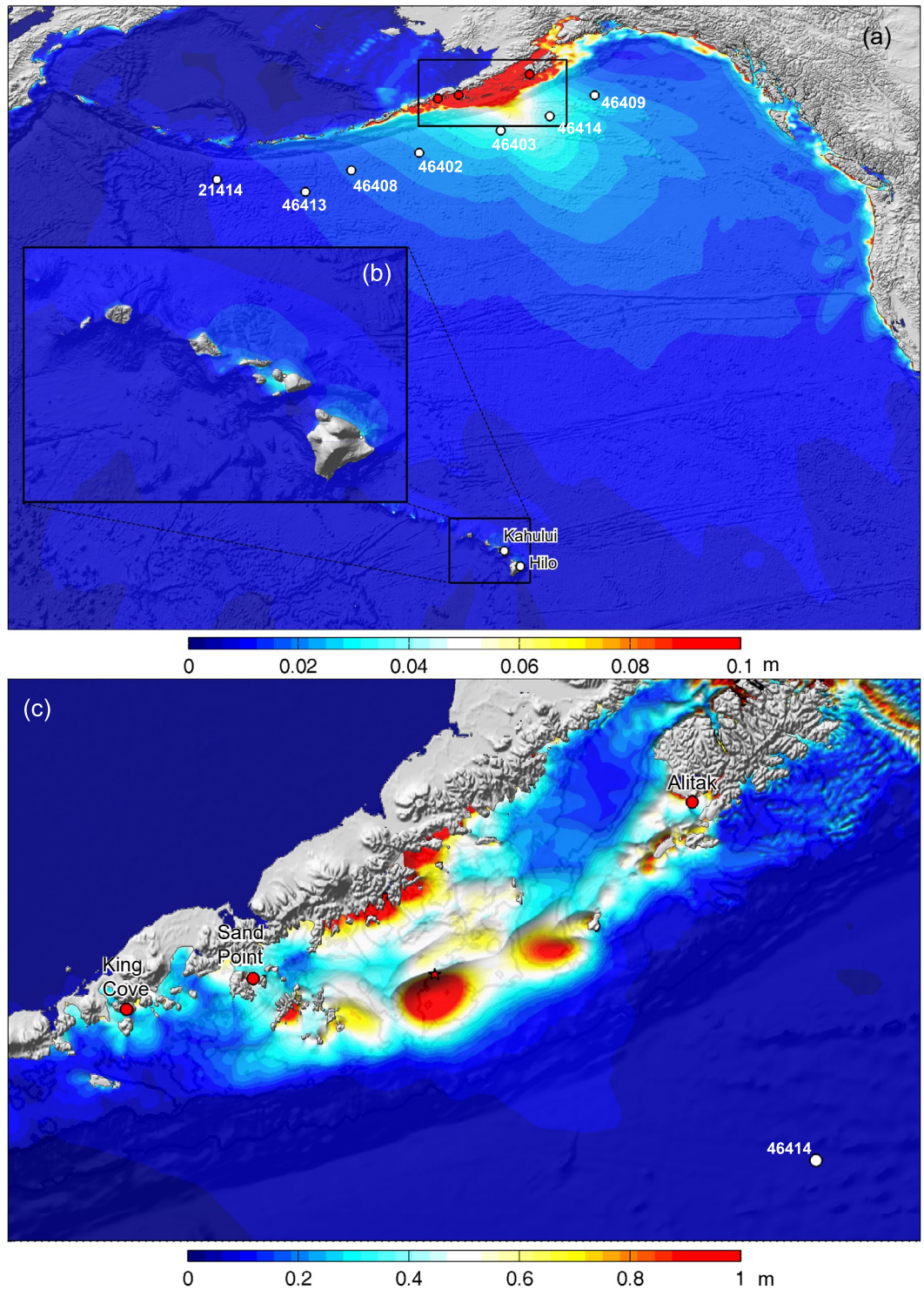

Figure 6. Computed tsunami wave amplitude. (a) Level-1 grid with outlines of level-2 grids denoted by rectangles. (b) Level-2 Hawaii grid. (c) Level-2 Alaska grid. Red star denotes the epicenter, and white and red circles, respectively, indicate locations of DART and tide gauge observations used in the iterative inversion and forward modeling.

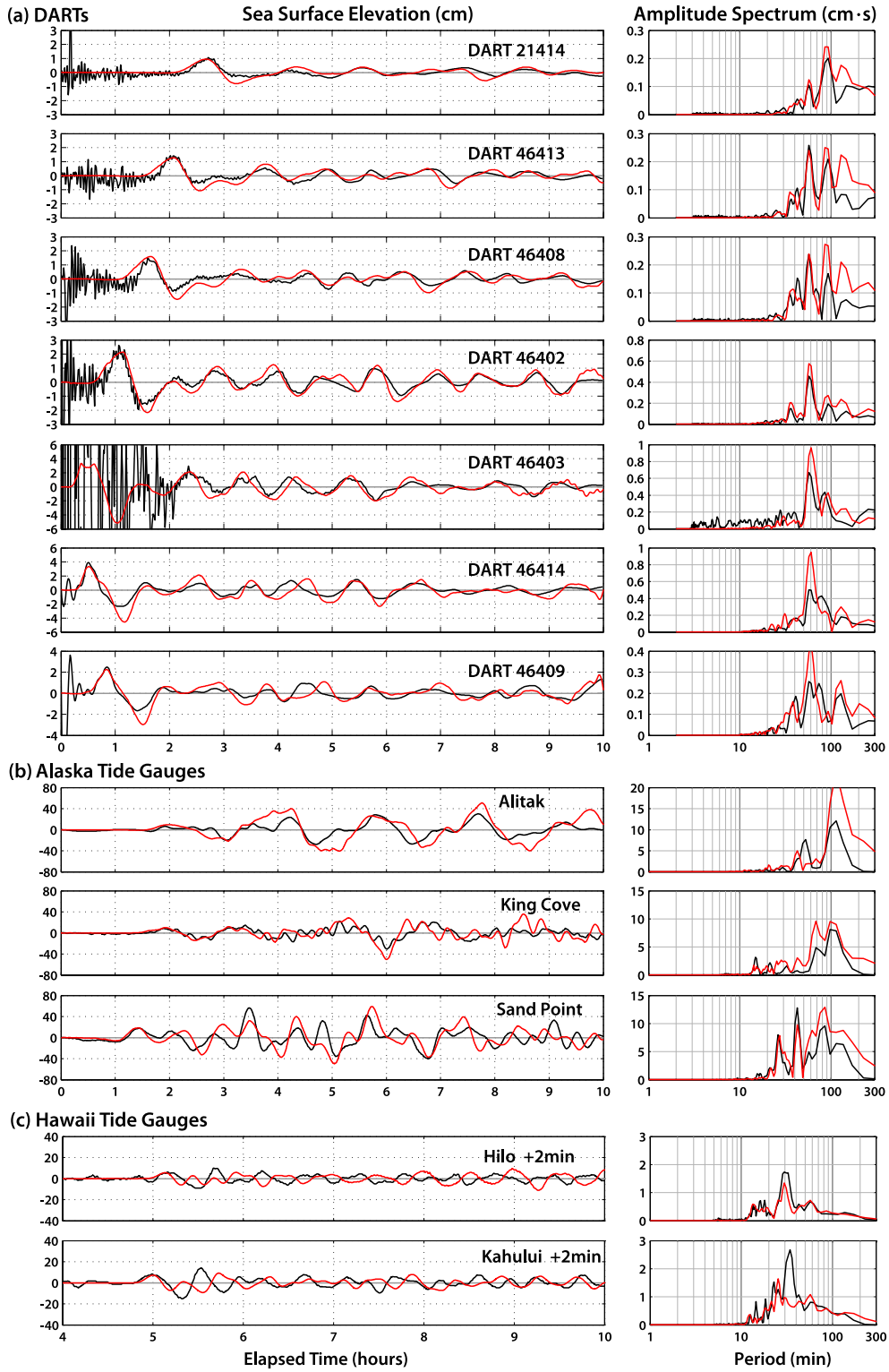

Figure 7. Comparison of observed (black) and computed (red) sea surface elevation time series and spectra for (a) DART stations, (b) Alaska tide gauges, and (c) Hawaii tide gauges. The observed DART signals were obtained by removing tidal signals and high-pass filtering the original recordings to suppress seismically induced excessive short-period signals. The computed signals from our preferred source model include only tsunami energy, so they do not predict the remaining short-period seismically induced signals.

break, the computed tsunamis from the Liu et al. (2022) model are too early for all DART stations and overpredict amplitudes (Figure S3 in Supporting Information S1; Mulia et al., 2022).

The basic features of these models are similar, and some differences are expected among finite-fault models that use different data sets and inversion algorithms. As an indication of the effects of modeling smoothing, Figure S4 in Supporting Information S1 shows the slip distributions for our final model configuration with different spatial smoothing factors of 0.1, 0.2, 0.5, and 1.0. Our preferred slip model uses a smoothing factor of 0.5. There is little variation in the predictions of seismic, geodetic, and tsunami data from these models. Due to the large depth extent, the coseismic surface deformation that controls the tsunami excitation is most sensitive to the spatial distribution and placement of slip and the total seismic moment, not the peak slip. Our successful iterative modeling of the seismic, geodetic, and tsunami data requires that slip not extend or produce seafloor uplift further seaward than in Figure 5, and any models that do so will likely violate the tsunami observations.

3.4. Aftershock Activity for the 2021 Chignik Event

All of the regional gCMT focal mechanisms for events from 1976 until 70 days after the 2021 event are shown in Figure 4a, highlighting the activity along-strike to the southwest associated with the 2020 Simeonof earthquake sequence and the relative paucity of activity within the large-slip areas of the 2021 rupture. The larger early aftershocks with gCMT solutions are concentrated in the region up-dip from the 2021 hypocenter where there is little coseismic slip. About six large events occurred near the 1938 hypocenter prior to 2021 (e.g., Ye et al., 2021). The USGS-Comcat earthquake locations within 4 months after the event are shown in Figure 4b. The continuing aftershock sequences beneath the Shumagin Islands and for the 19 October 2021 M_W 7.6 intraplate aftershock seaward of the 2020 M_W 7.8 event are evident, with very little seismicity between the 2021 rupture zone and the Shumagin Islands. Most early aftershock activity for the 2021 Chignik event is located up-dip of the large-slip zone, primarily from 16-km to 25-km depth, with a concentration in the region up-dip from the large-slip zone along the hypocenter (Figure S1 in Supporting Information S1). Several patches of aftershocks are located beneath the continental slope. If the early aftershocks were used to define the rupture area, it would significantly overestimate the rupture zone and suggest that coseismic faulting occurred further up-dip than is the actual case. This same caveat likely applies to the 1938 aftershock zone shown in Figure 1, compounded by much larger aftershock location uncertainties for those events. The spatial distribution of aftershocks for the 2021 event is hard to compare with that for the 1938 event, due to the sparseness (13 poorly located events) of the latter.

An attribute of the 2021 aftershock distribution that can be compared with other megathrust ruptures is the aftershock productivity (e.g., Dascher-Cousineau et al., 2020; Ye et al., 2021). Using the procedure for counting aftershocks in a fixed space-time window adopted by Ye et al. (2021), we count the total number of shallow aftershocks with $m_B \geq 4.5$ in a 45-day window after the main event within a radius of 500 km from the USGS-NEIC epicenter, finding 32 events, 5 of which are outside the Semidi segment and can probably be disregarded. The aftershock productivity of 27–32 events is low compared with a predicted number of 194 for an 8.2 event using the average relationship found for shallow earthquakes larger than magnitude 7.0 by Ye et al. (2020). The 2021 event is consistent with the tendency for continental subduction zones in the eastern Pacific to have lower productivity than island arcs of the western Pacific (e.g., Singh & Suárez, 1988; Wetzler et al., 2016), but the value is particularly low given that it included an M_W 6.9 aftershock on 14 August 2021. A low b-value for seismicity in the decade before the event in the western portion of the Semidi segment was noted by Liu et al. (2020), so there may be localized properties of the megathrust that reduces background and aftershock activity. It has been noted that the Zodiak Fan (e.g., Stevenson et al., 1983; von Huene et al., 2012), a thick sedimentary deposit on the Pacific plate is subducting in the Semidi segment, and this could provide anomalous properties in the fault zone.

3.5. Magnitude (M_S, m_B) and Waveform Comparison With the 1938 Event

The 1938 event occurred when seismic stations with limited bandwidth and dynamic range were operational, and there were no geodetic or deep-sea ocean bottom pressure measurements to constrain the ground deformation. Surface-wave magnitude, M_S, measurements for about 20-s period are available (Di Giacomo & Storchak, 2022), and these are compared with M_S measurements from global broadband stations for the 2021 event (Figure 8). The azimuthal distribution for modern instruments is good and demonstrates that there can be substantial variations in magnitudes with azimuth, so one must be cautious in interpreting the sparse data for 1938. The ISC assigns

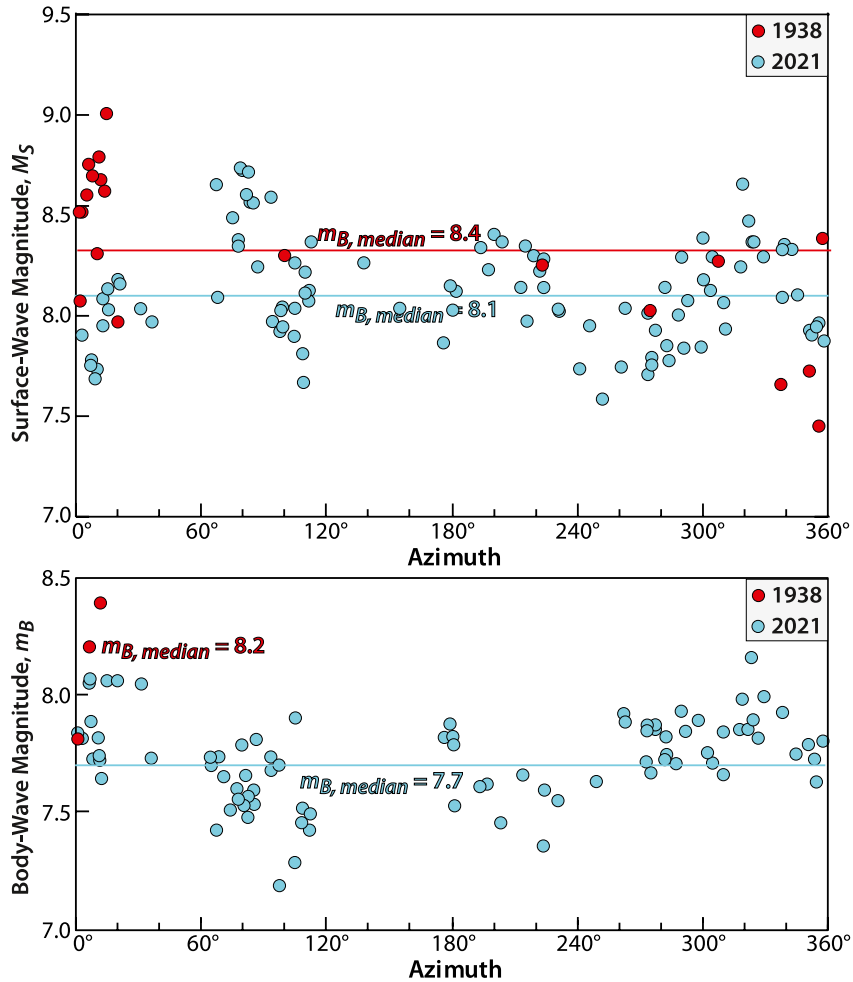

Figure 8. Comparison of surface-wave magnitude M_S (top) and body-wave magnitude m_B (bottom) measurements for the 2021 (cyan) and 1938 (red) Alaska earthquakes along the Semidi segment. The 2021 M_S measurements are from vertical component recordings, whereas the 1938 measurements are taken from Di Giacomo and Storchak (2021). The median M_S value for the 2021 event is 8.1, whereas the ISC reports M_S of 8.39 for the 1938 event. Gutenberg and Richter (1954) and Abe (1981) assign the 1938 event M_S 8.3. The m_B values for 2021 have a median of 7.7, with a median period of 4.1 s, following the procedure of Kanamori and Ross (2019). The three m_B values for 1938 are from the Gutenberg Notepads (Goodstein et al., 1980), and have a median value of 8.2 (Abe, 1981).

M_S = 8.39 to the 1938 event, while Gutenberg and Richter (1954) and Abe (1981) assign it M_S = 8.3, whereas the median M_S for the 2021 event is 8.1. The values for stations at northern azimuths are larger for 1938 than for 2021, so the magnitude difference for common paths is suggestive, but the overall scatter is such that the events are best viewed as roughly comparable in 20 s source strength.

Broadband Gutenberg body-wave magnitude m_B measurements for the two events are shown in Figure 8 as well, with measurements from only three stations reported for the 1938 event in the Gutenberg notepads (Goodstein et al., 1980). Abe (1981) assigned the event a Gutenberg m_B = 8.2. These values are all for northerly azimuths as well, and this is an unusually large m_B for the classic measurement. The 2021 values at northerly azimuths do have some measures, following the procedure of Kanamori and Ross (2019), larger than 8.0, with the median over all azimuths being 7.7 (for a median period of 4.1 s). Comparison of values in the same azimuth range again is suggestive of a larger size for the 1938 event at periods of 4–5 s, but the data could be influenced by greater directivity effects for the 1938 rupture or a different slip pattern, so the events are at least comparable in source strength at this period.

Direct comparison of waveforms recorded by the 1938 and 2021 events is rather challenging, as the handful of stations for which *P* and *S* waveforms were modeled by Estabrook et al. (1994) involved instrument types that

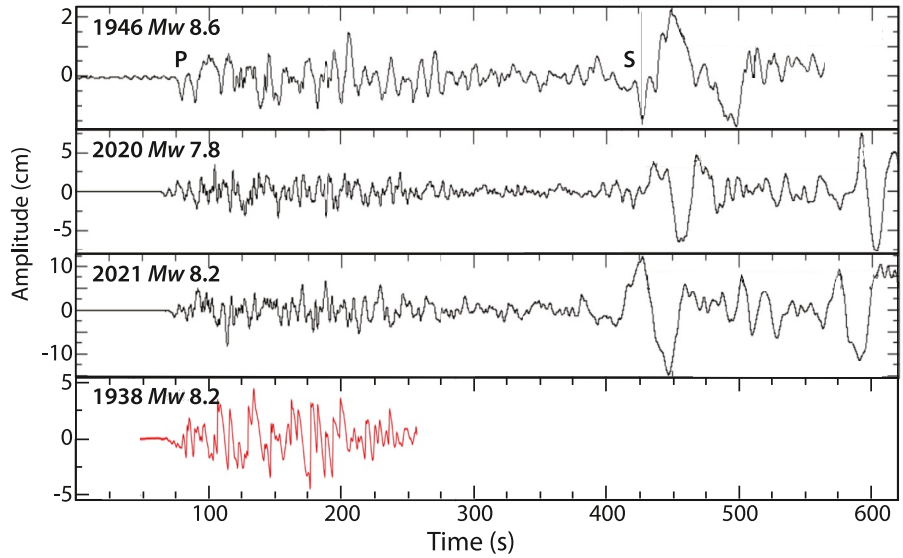

Figure 9. Comparison of *P* and *S* waves (*P* only for the 1938 event) recorded at station PAS (Pasadena, CA) for the four largest events shown in Figure 1. The instrument response is for the long-period (1–90 s) Benioff vertical component with a gain of 3,000. The 1938 and 1946 waveforms are from Hartzell and Heaton (1985). Note the variation in vertical scales. The *P* waves for the 1946 tsunami earthquake have significantly longer period than for the three deeper megathrust events. The 1938 *P* wave has the largest arrivals >60 s after the first arrival that are not apparent for the 2021 event.

are no longer operating. Unspecified, but rather severe, low-pass filtering of the waveforms shown in their paper made it ambiguous to compare with nearby recordings for the 2021 event for which broadband records could be passed through corresponding instrument responses. The one station for which we have high confidence in the signals is PAS (Pasadena, California), which recorded the 1938 event on a long-period Benioff (1–90 s) vertical component seismometer with a gain of 3,000 (Hartzell & Heaton, 1985). We compare the *P* recordings for the 1938 and 1946 earthquakes with broadband signals at PAS convolved with the long-period Benioff response for the 2020 M_W 7.8 Simeonof and 2021 M_W 8.2 Chignik events (Figure 9).

The peak amplitudes in the *P* wave are comparable for the 1938 and 2021 events, but there is a notably larger set of arrivals ~60 s after the first *P* arrival for the 1938 event. This feature was noted in other waveforms for the 1938 earthquake by Estabrook et al. (1994) and prompted their two-subevent models of the earthquake where the second, larger subevent begins 60 s after the first arrival located 178-km along-strike to the northeast (Figure 10b). The 2021 M_W 8.2 Chignik event has larger *P* and *S* amplitudes than for the 2020 M_W 7.8 Simeonof earthquake at PAS, confirming that this waveform comparison is sensible. The 1946 event has distinctly longer period energy in the first 200 s of the complex *P* wave train, consistent with the long source process time that characterized as a slow rupturing earthquake (Kanamori, 1972). The likely shallow source of the 1946 tsunami earthquake (e.g., Okal & Hébert, 2007) is probably associated with the distinct waveform attributes that are not observed for the deeper 2021 event.

3.6. MRF and Slip Distribution Comparison With the 1938 Event

The limited *P* and *S* seismic data available for the 1938 event were modeled by Estabrook et al. (1994). The MRF of their two-subevent model shows the strong moment rate after 60 s (Figure 10a) which results from late large *P* energy like that seen at PAS (Figure 9). The 1938 MRF directly obtained by deconvolution of the *P* wave signal at PAS by Hartzell and Heaton (1985) also has two large pulses from 50 to 100 s, clearly distinct from the 2021 MRF for our preferred model (Figure 10a). This provides strong evidence for the 1938 and 2021 ruptures having different slip distributions and the two events not being simple repeat failures.

A summary of the inferred rupture attributes for the 1938 event from seismic (Estabrook et al., 1994) and tsunami modeling (Freymueller et al., 2021; Johnson & Satake, 1994) is compared with an outline of the large-slip (>2 m) zone for the 2021 event (Figure 10b). Both the seismic and tsunami representations of the 1938 event indicate

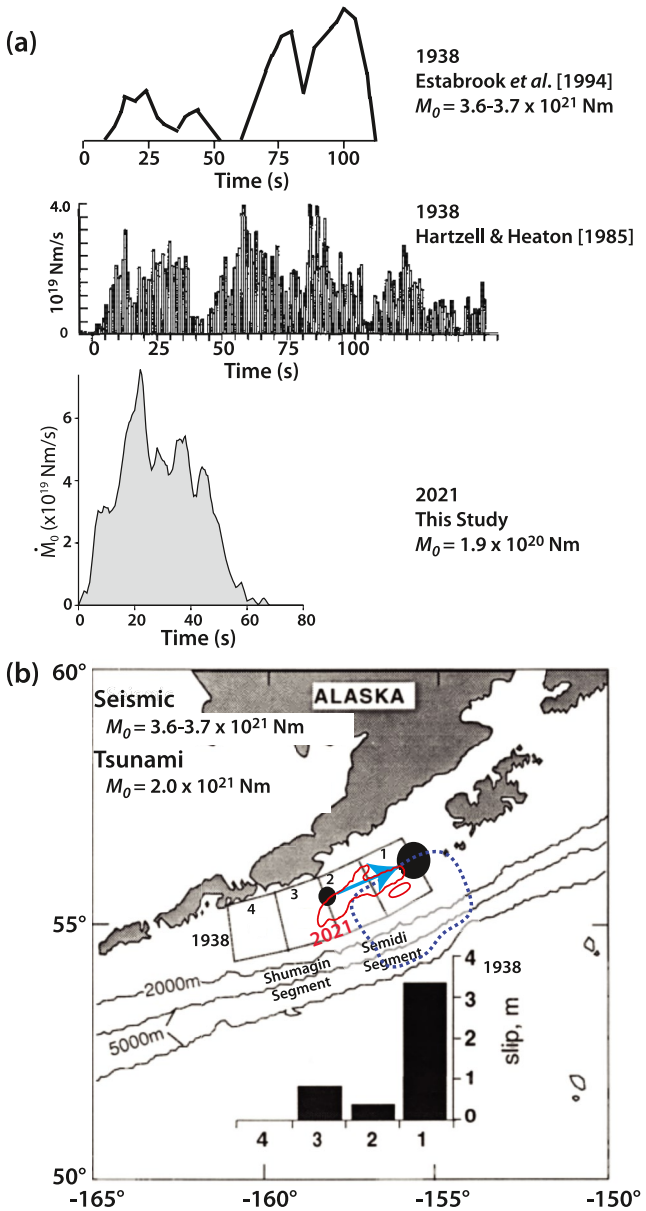

Figure 10. (a) Moment-rate functions (MRFs) for the 1938 and 2021Alaska earthquakes in the Semidi segment. The 1938 MRFs are from a two-subevent inversion by Estabrook et al. (1994), which used five *P* waves and four *SH* waves, and a single-station deconvolution of the PAS long-period Benioff recording shown in Figure 9 by Hartzell and Heaton (1985). Both MRFs show large moment between 50 and 100 s, whereas the MRF for the 2021 event from our preferred slip model (Figure 2) has no significant moment rate after 60 s. (b) Summary of the 1938 finite-source estimates. Two-subevent inversion by Estabrook et al. (1994) is indicated by two circles 178 km apart, scaled proportional to the seismic moment, with the cyan arrow indicating the rupture direction. The four-segment tsunami source model of Johnson and Satake (1994) with the uniform slip in each segment is indicated by the histograms and four grids (1, 2, 3, and 4) in the map. The dark blue dashed outline shows the large-slip region in the preferred "far eastern" tsunami source model of Freymueller et al. (2021). The red outline shows the main slip zone for the 2021 event (Figure 1).

a large slip extending well east of the 2021 rupture zone. There was little or no slip in the Shumagin segment during the 1938 and 2021 ruptures. The seismic data for 1938 does not allow for detailed spatial slip characterization, and its source models have a different up-dip extent of rupture based on the fitting of a limited number of tide gauge recordings, so the details of the 1938 rupture are not well resolved. However, it is not clear that the 1938 rupture really reached to the trench as indicated in the preferred model of Freymueller et al. (2021). If it did, it is very distinct from the 2021 event where rupture was confined to below the continental shelf (Figure 3). Given the greatly enhanced seaward radiation of tsunami when uplift occurs in deeper water above the continental slope, and the reasonable fit obtained to data in Hawaii and California by the deeper slip modeling of Johnson and Satake (1994), we are performing further modeling to evaluate this issue.

The above comparisons indicate that the 1938 and 2021 ruptures are significantly different in spatial slip distribution. The question on the persistence of large-slip regions (asperities) through cycles of repeated failure of megathrust segments has long been of interest (e.g., Kobayashi et al., 2020; Schwartz, 1999; Tilmann et al., 2016; Ye, Kanamori, et al., 2016), but the number of well-constrained slip distributions for re-ruptures of a given region in great earthquakes remains very limited. While the 1938 and 2021 rupture zones overlap, even within that subregion it is not possible to confidently identify a persistent asperity slip patch.

The well-resolved up-dip limit of coseismic slip for the 2021 M_W 8.2 Chignik earthquake indicates that the megathrust region below the continental slope did not experience slip in the mainshock, similar to the 2020 M_W 7.8 Simeonof earthquake (Figure 1). The area of the megathrust that extends from 25-km depth to the trench is substantial, likely comparable to that failed in the 1946 tsunami earthquake (e.g., Okal & Hébert, 2007; von Huene et al., 2016, 2021). However, it is presently unknown whether the shallow megathrust has significant slip deficit accumulation or has undergone an afterslip for the 2021 event. The structure in the toe reveals multiple thrust faults in the sediments indicating compressional contraction (e.g., Li et al., 2015, 2018), and the thick sediment package of the Zodiak Fan has partially subducted in this region (von Huene et al., 2012). The aftershocks of the 2021 event occurred only in limited regions beneath the continental slope (Figure 3b), the seismogenic characteristics of the toe remain highly uncertain.

4. Conclusions

The 29 July 2021 M_W 8.2 Chignik thrust earthquake ruptured the down-dip part of the megathrust in the Semidi segment, with two large-slip patches distributed over a total of ~170-km along-strike. Slip only occurred beneath the continental shelf, with tsunami observations providing key constraints on the up-dip extent of slip. Early aftershocks are concentrated up-dip of the slip zone, particularly in the western portion of the rupture, but these also do not extend to the trench, although several patches of aftershocks are located beneath the continental slope. The 2021 rupture spans about two-thirds of the 1938 aftershock zone, but available seismic and tsunami information shows that the 1938 rupture lasted much longer, extended further northeast, beyond the Semidi Islands, and had more slip in the eastern portion of the rupture than in the west. This indicates that the 1938 and 2021 events are not simple re-ruptures of persistent asperities, and the eastern portion of the

1938 zone still has potential for a large slip deficit to have persisted after the 2021 event. The up-dip region of the megathrust beneath the continental slope has uncertain frictional properties and may or may not have significant slip deficit. Continued monitoring for shallow afterslip in the up-dip region might address this issue, although the land-based geodetic data are far from the region of concern and may fail to detect slip deficit, as appears to be the case for the region of the 1946 tsunami earthquake, which shows no slip deficit in the available GNSS stations on the Alaska Peninsula. Seafloor geodesy may help to address the shallow deformation.

Data Availability Statement

Earthquake information are based on the catalogs from the US Geological Survey National Earthquake Information Center (USGS-NEIC) (https://earthquake.usgs.gov/earthquakes). All seismic data were downloaded through the IRIS Wilber 3 system (https://ds.iris.edu/wilber3/) with stations from Global Seismographic Network (II: https://doi.org/10.7914/SN/II, IU: https://doi.org/10.7914/SN/IU), and International Federation of Digital Seismic Networks (FDSN; AU: https://doi.org/10.26186/144675, AZ: https://doi.org/10.7914/SN/AZ, C1: https://doi.org/10.7914/SN/C1, CI: https://doi.org/10.7914/SN/CI, CM: https://doi.org/10.7914/SN/CM, CN: https://doi.org/10.7914/SN/CN, CU: https://doi.org/10.7914/SN/CU, DK, G: https://doi.org/10.18715/GEOSCOPE.G, GE: https://doi.org/10.14470/TR560404, IC: https://doi.org/10.7914/SN/IC, and JP). We thank the facilities of IRIS Data Services, and specifically the IRIS Data Management Center, which were used for access to waveforms, related metadata, and/or derived products used in this study. IRIS Data Services are funded through the Seismological Facilities for the Advancement of Geoscience (SAGE) Award of the National Science Foundation under Cooperative Support Agreement EAR-1851048. Coseismic static GNSS displacements were obtained from the UNAVCO Bulletin Board (https://www.unavco.org/event-response/july-28-2021-m-8-2-alaska-earthquake/).

Acknowledgments
We thank editor Rachel Abercrombie, associate editor Alice-Agnes Gabriel, reviewer Ronni Grapenthin, and an anonymous reviewer for helpful comments on the manuscript. The GNSS data are based on the services provided by the GAGE Facility, operated by UNAVCO, Inc., with support from the National Science Foundation and the National Aeronautics and Space Administration under NSF Cooperative Agreement EAR-1724794. The high-resolution digital elevation model, Sand Point V2, at the Shumagin Islands was downloaded from the Nation Centers for Environmental Information (https://maps.ngdc.noaa.gov/viewers/bathymetry/). Lingling Ye's earthquake study was supported by the National Natural Science Foundation of China (No. 41874056). Yefei Bai's tsunami research was supported by the Finance Science and Technology Project of Hainan Province (No. ZDKJ202019). Thorne Lay's earthquake research was supported by the National Science Foundation (Grant EAR1802364).

References

Abe, K. (1981). Magnitudes of large shallow earthquakes from 1904 to 1980. *Physics of the Earth and Planetary Interiors*, *27*, 72–92. https://doi.org/10.1016/0031-9201(81)90088-1

Bai, Y., Cheung, K. F., Yamazaki, Y., Lay, T., & Ye, L. (2014). Tsunami surges around the Hawaiian islands from the 1 April 2014 North Chile M_W 8.1 earthquake. *Geophysical Research Letters*, *41*, 8512–8521. https://doi.org/10.1002/2014GL061686

Bai, Y., Liu, C., Lay, T., Cheung, K. F., & Ye, L. (2022). Optimizing a model of coseismic rupture for the 22 July 2020 Mw 7.8 Simeonof earthquake by exploiting acute sensitivity of tsunami excitation across the shelf break. *Journal of Geophysical Research: Solid Earth*, *127*, e2022JB024484. https://doi.org/10.1029/2022JB024484

Bai, Y., Ye, L., Yamazaki, Y., Lay, T., & Cheung, K. F. (2018). The 4 May 2018 MW 6.9 Hawaii Island earthquake and implications for tsunami hazards. *Geophysical Research Letters*, *45*, 11040–11049. https://doi.org/10.1029/2018GL079742

Blewitt, G., Hammond, W. C., & Kreemer, C. (2018). Harnessing the GPS data explosion for interdisciplinary science. *Eos, Transactions American Geophysical Union*, *99*. https://doi.org/10.1029/2018EO104623

Boyd, T. M., & Lerner-Lam, A. L. (1988). Spatial distribution of turn-of-the-century seismicity along the Alaska-Aleutian arc. *Bulletin of the Seismological Society of America*, *78*(2), 636–650.

Briggs, R. W., Engelhart, S. E., Nelson, A. R., Dura, T., Kemp, A. C., Haeussler, P. J., et al. (2014). Uplift and subsidence reveal a nonpersistent megathrust rupture boundary (Sitkinak Island, Alaska). *Geophysical Research Letters*, *41*, 2289–2296. https://doi.org/10.1002/2014GL059380

Cheung, K. F., Bai, Y., & Yamazaki, Y. (2013). Surges around the Hawaiian islands from the 2011 Tohoku tsunami. *Journal of Geophysical Research: Oceans*, *119*, 5703–5719. https://doi.org/10.1002/jgrc.20413

Convers, J. A., & Newman, A. V. (2011). Global evaluation of large earthquake energy from 1997 through mid-2010. *Journal of Geophysical Research*, *116*, B08304. https://doi.org/10.1029/2010JB007928

Cross, R. S., & Freymueller, J. T. (2008). Evidence for and implications of a Bering plate based on geodetic measurements from the Aleutians and Western Alaska. *Journal of Geophysical Research*, *113*, B07405. https://doi.org/10.1029/2007JB005136

Crowell, B. W., & Melgar, D. (2020). Slipping the Shumagin gap: A kinematic coseismic and early afterslip model of the M_W 7.8 Simeonof Island, Alaska, earthquake. *Geophysical Research Letters*, *47*, e2020GL090308. https://doi.org/10.1029/2020GL090308

Dascher-Cousineau, K., Brodsky, E. E., Lay, T., & Goebel, T. H. W. (2020). What controls variations in aftershock productivity? *Journal of Geophysical Research: Solid Earth*, *125*, e2019JB018111. https://doi.org/10.1029/2019JB018111

Davies, J., Sykes, L., House, L., & Jacob, K. (1981). Shumagin seismic gap, Alaska Peninsula: History of great earthquakes, tectonic setting, and evidence for high seismic potential. *Journal of Geophysical Research*, *86*(B5), 3821–3855. https://doi.org/10.1029/JB086iB05p03821

DeMets, C., Gordon, R. G., & Argus, D. F. (2010). Geologically current plate motions. *Geophysical Journal International*, *181*, 1–80. https://doi.org/10.1111/j.1365-246x.2009.04491.x

Di Giacomo, D., & Storchak, D. A. (2021). 100+ years of recomputed surface wave magnitudes of shallow earthquakes. *Earth System Science Data Discussions*, 1–37. https://doi.org/10.5194/essd-2021-266

Di Giacomo, D., & Storchak, D. A. (2022). One hundred plus years of recomputed surface wave magnitude of shallow global earthquakes. *Earth System Science Data*, *14*(2), 393–409. https://doi.org/10.5194/essd-14-393-2022

Droof, C., & Freymueller, J. T. (2021). New constraints on slip deficit on the Aleutian megathrust and inflation at Mt. Veniamino, Alaska from repeat GPS measurements. *Geophysical Research Letters*, *48*, e2020GL091787. https://doi.org/10.1029/2020GL091787

Elliott, J. L., Grapenthin, R., Parameswaran, R. M., Xiao, Z., Freymueller, J. T., & Fusso, L. (2022). Cascading rupture of a megathrust. *Science Advances*, *8*(18), eabm4131. https://doi.org/10.1126/sciadv.abm4131

Estabrook, C. H., & Boyd, T. M. (1992). The Shumagin Islands, Alaska, earthquake of 31 May 1917. *Bulletin of the Seismological Society of America*, *82*(2), 755–773.

Estabrook, C. H., Jacob, K. H., & Sykes, L. R. (1994). Body wave and surface wave analysis of large and great earthquakes along the Eastern Aleutian Arc, 1923–1993: Implications for future events. *Journal of Geophysical Research*, *995*, 11643–11662. https://doi.org/10.1029/93JB03124

Fletcher, H. J., Beavan, J., Freymueller, J., & Gilbert, L. (2001). High interseismic coupling of the Alaska subduction zone SW of Kodiak Island inferred from GPS data. *Geophysical Research Letters*, *28*, 443–446. https://doi.org/10.1029/2000GL012258

Fournier, T. J., & Freymueller, J. T. (2007). Transition from locked to creeping subduction in the Shumagin region, Alaska. *Geophysical Research Letters*, *34*, L06303. https://doi.org/10.1029/2006GL029073

Freymueller, J. T., & Beavan, J. (1999). Absence of strain accumulation in the Western Shumagin segment of the Alaska subduction zone. *Geophysical Research Letters*, *26*, 3233–3236. https://doi.org/10.1029/1999GL008356

Freymueller, J. T., Suleimani, E. N., & Nicolsky, D. J. (2021). Constraints on the slip distribution of the 1938 M_W 8.3 Alaska Peninsula earthquake from tsunami modeling. *Geophysical Research Letters*, *48*, e2021GL092812. https://doi.org/10.1029/2021GL092812

Freymueller, J. T., Woodard, H., Cohen, S. C., Cross, R., Elliott, J., Larsen, C. F., et al. (2008). Active deformation processes in Alaska, based on 15 years of GPS measurements. In J. T.Freymueller, P. J.Haeussler, R. L.Wesson, & G.Ekström (Eds.), *Active tectonics and seismic potential of Alaska* (Vol. 179, pp. 1–42). https://doi.org/10.1029/179GM02

Goodstein, J. R., Kanamori, H., & Lee, W. (1980). Seismology microfiche publications from the caltech archive. *Bulletin of the Seismological Society of America*, *70*, 657–658.

Gutenberg, B., & Richter, C. F. (1954). *Seismicity of the Earth and associated phenomena* (2nd ed., p. 310). Princeton University Press.

Hartzell, S. H., & Heaton, T. H. (1983). Inversion of strong ground motion and teleseismic waveform data for the fault rupture history of the 1979 Imperial Valley California, earthquake. *Bulletin of the Seismological Society of America*, *73*(6A), 1553–1583. https://doi.org/10.1785/bssa07306a1553

Hartzell, S. H., & Heaton, T. H. (1985). Teleseismic time functions or large, shallow subduction zone earthquakes. *Bulletin of the Seismological Society of America*, *75*, 965–1004.

Hayes, G. P., Moore, G. L., Portner, D. E., Hearne, M., Flamme, H., Furtney, M., & Smoczyk, G. M. (2018). Slab2, a comprehensive subduction zone geometry model. *Science*, *362*(6410), 58–61. https://doi.org/10.1126/science.aat4723

Heidarzadeh, M., Murotani, S., Satake, K., Ishibe, T., & Gusman, A. R. (2016). Source model of the 16 September 2015 Illapel, Chile, M_W 8.4 earthquake based on teleseismic and tsunami data. *Geophysical Research Letters*, *43*, 643–650. https://doi.org/10.1002/2015GL067297

Johnson, J. M., & Satake, K. (1994). Rupture extent of the 1938 Alaskan earthquake as inferred from tsunami waveforms. *Geophysical Research Letters*, *21*, 733–736. https://doi.org/10.1029/94GL00333

Kanamori, H. (1972). Mechanism of tsunami earthquakes. *Physics of the Earth and Planetary Interiors*, *6*, 346–359. https://doi.org/10.1016/0031-9201(72)90058-1

Kanamori, H., & Rivera, L. (2008). Source inversion of *W* phase: Speeding up seismic tsunami warning. *Geophysical Journal International*, *175*, 222–238. https://doi.org/10.1111/j.1365-246x.2008.03887.x

Kanamori, H., & Ross, Z. E. (2019). Reviving m_B. *Geophysical Journal International*, *216*, 1798–1816. https://doi.org/10.1093/gji/ggy510

Kikuchi, M., & Kanamori, H. (1991). Inversion of complex body waves—III. *Bulletin of the Seismological Society of America*, *81*(6), 2335–2350. https://doi.org/10.1785/bssa0810062335

Kobayashi, H., Koketsu, K., Miyake, H., & Kanamori, H. (2020). Similarities and differences in the rupture processes of the 1952 and 2003 Tokach-oki earthquakes. *Journal of Geophysical Research: Solid Earth*, *126*, e2020JB020585. https://doi.org/10.1029/2020JB020585

Kuehn, H. (2019). *Along-trench segmentation and down-dip limit of the seismogenic zone at the eastern Alaska-Aleutian subduction zone (Ph.D. thesis)*. Dalhousie University.

Li, J., Shillington, D. J., Bécel, A., Nedimović, M. R., Webb, S. C., Saffer, D. M., et al. (2015). Downdip variations in seismic reflection character: Implications for fault structure and seismogenic behavior in the Alaska subduction zone. *Journal of Geophysical Research: Solid Earth*, *120*, 7883–7904. https://doi.org/10.1002/2015JB012338

Li, J., Shillington, D. J., Saffer, D. M., Bécel, A., Nedimović, M. R., Kuehn, H., et al. (2018). Connections between subducted sediment, pore-fluid pressure, and earthquake behavior along the Alaska megathrust. *Geology*, *46*(4), 299–302. https://doi.org/10.1130/G39557.1

Li, L., & Cheung, K. F. (2019). Numerical dispersion in non-hydrostatic modeling of long-wave propagation. *Ocean Modelling*, *138*, 68–87. https://doi.org/10.1016/j.ocemod.2019.05.002

Li, L., Lay, T., Cheung, K. F., & Ye, L. (2016). Joint modeling of teleseismic and tsunami wave observations to constrain the 16 September 2015 Illapel, Chile, M_W 8.3 earthquake rupture process. *Geophysical Research Letters*, *43*, 4303–4312. https://doi.org/10.1002/2016GL068674

Li, S., & Freymueller, J. T. (2018). Spatial variation of slip behavior beneath the Alaska Peninsula along Alaska-Aleutian subduction zone. *Geophysical Research Letters*, *45*, 3453–3460. https://doi.org/10.1002/2017GL076761

Liu, C., Lay, T., & Xiong, X. (2022). The 29 July 2021 M_W 8.2 Chignik, Alaska Peninsula earthquake rupture inferred from seismic and geodetic observations: Re-Rupture of the Western 2/3 of the 1938 rupture zone. *Geophysical Research Letters*, *49*, e2021GL096004. https://doi.org/10.1029/2021GL096004

Liu, C., Lay, T., Xiong, X., & Wen, Y. (2020). Rupture of the 2020 M_W 7.8 earthquake in the Shumagin gap inferred from seismic and geodetic observations. *Geophysical Research Letter*, *47*, e2020GL090806. https://doi.org/10.1029/2020GL090806

Mulia, I. E., Gusman, A., Heidarzadeh, M., & Satake, K. (2022). Sensitivity of tsunami data to the up-dip extent of the July 2021 Mw 8.2 Alaska earthquake. *Seismological Research Letters*, *93*(4), 1992–2003. https://doi.org/10.1785/0220210359

Nelson, A. R., Briggs, R. W., Dura, T., Engelhart, S. E., Gelfenbaum, G., Bradley, L.-A., et al. (2015). Tsunami recurrence in the eastern Alaska-Aleutian arc: A Holocene stratigraphic record from Chirikof Island, Alaska. *Geosphere*, *11*(4), 1172–1203. https://doi.org/10.1130/GES01108.1

Okada, Y. (1985). Surface deformation due to shear and tensile faults in a half-space. *Bulletin of the seismological society of America*, *75*(4), 1135-1154.

Okal, E. A., & Hébert, H. (2007). Far-field simulation of the 1946 Aleutain tsunami. *Geophysical Journal International*, *169*, 1229–1238. https://doi.org/10.1111/j.1365-246x.2007.03375.x

Romano, F., Lorito, S., Lay, T., Piatanesi, A., Volpe, M., Murphy, S., & Tonini, R. (2020). Benchmarking the Optimal Time Alignment (OTA) of tsunami waveforms in nonlinear joint inversions for the M_W 8.8 2010 Maule (Chile) earthquake. *Frontiers of Earth Science*, *8*, 585429. https://doi.org/10.3389/feart.2020.585429

Schwartz, S. Y. (1999). Noncharacteristic behavior and complex recurrence of large subduction zone earthquakes. *Journal of Geophysical Research*, *104*(B10), 23111–23125. https://doi.org/10.1029/1999JB900226

Singh, S. K., & Suárez, G. (1988). Regional variation in the number of aftershocks ($m_b \geq 5$) of large, subduction-zone earthquakes ($M_W \geq 7.0$). *Bulletin of the Seismological Society of America*, *78*, 230–242.

Stevenson, A. J., Scholl, D. W., & Vallier, T. L. (1983). Tectonic and geologic implications of the Zodiak Fan, Aleutian abyssal plain, northeast Pacific. *The Geological Society of America Bulletin*, *94*, 259–273. https://doi.org/10.1130/0016-7606(1983)94<259:tagiot>2.0.co;2

Sykes, L. R. (1971). Aftershock zones of great earthquakes, seismicity gaps, earthquake prediction for Alaska and the Aleutians. *Journal of Geophysical Research*, *76*, 8021–8041. https://doi.org/10.1029/JB076i032p08021

Sykes, L. R., Kisslinger, J. B., House, L., Davies, J. N., & Jacob, K. H. (1981). Rupture zones of great earthquakes in the Alaska-Aleutian arc, 1784 to 1980. *Science*, *210*(4476), 1343–1345.

Tanioka, Y., & Satake, K. (1996). Tsunami generation by horizontal displacement of ocean bottom. *Geophysical Research Letters*, *23*, 861–864. https://doi.org/10.1029/96GL00736

Tilmann, F., Zhang, Y., Moreno, M., Saul, J., Eckelmann, F., Palo, M., et al. (2016). The 2015 Illapel earthquake, central Chile: A type case for a characteristic earthquake? *Geophysical Research Letters*, *43*, 574–583. https://doi.org/10.1002/2015GL066963

USGS. (2013). *Alaska earthquake source for the SAFRR tsunami scenario*. In *Open-File Report 2013-1170-B* (Vol. 229). California Geological Survey Special Report.

von Huene, R., Miller, J. J., & Dartnell, P. (2016). A possible transoceanic tsunami directed toward the US west coast from the Semidi segment, Alaska convergent margin. *Geochemistry, Geophysics, Geosystems*, *17*, 645–659. https://doi.org/10.1002/2015GC006147

von Huene, R., Miller, J. J., & Krabbenhoeft, A. (2021). The Alaska convergent margin backstop splay fault zone, a potential large tsunami generator between the frontal prism and continental framework. *Geochemistry, Geophysics, Geosystems*, *22*, e2019GC008901. https://doi.org/10.1029/2019GC008901

von Huene, R., Miller, J. J., & Weinrebe, W. (2012). Subducting plate geology in three great earthquake ruptures of the Western Alaska margin, Kodiak to Unimak. *Geosphere*, *8*, 628–644. https://doi.org/10.1130/ges00715.1

Wetzler, N., Brodsky, E. E., & Lay, T. (2016). Regional and stress drop effects on aftershock productivity of large megathrust earthquakes. *Geophysical Research Letters*, *43*, 12012–12020. https://doi.org/10.1002/2016GL071104

Wetzler, N., Lay, T., Brodsky, E. E., & Kanamori, H. (2018). Systematic deficiency of aftershocks in areas of high coseismic slip for large subduction zone earthquakes. *Science Advances*, *4*, eaao3225. https://doi.org/10.1126/sciadv.aao3225

Witter, R. C., Briggs, R. W., Engelhart, S. E., Gelfenbaum, G., Koehler, R. D., & Barnhart, W. D. (2014). Little late Holocene strain accumulation and release on the Aleutian megathrust below the Shumagin Islands, Alaska. *Geophysical Research Letters*, *41*, 2359–2367. https://doi.org/10.1002/2014GL059393

Xiao, Z., Freymueller, J. T., Grapenthin, R., Elliott, J. L., Drooff, C., & Fusso, L. (2021). The deep Shumagin gap filled: Kinematic rupture model and slip budget analysis of the 2020 Mw 7.8 Simeonof earthquake constrained by GNSS, global seismic waveforms, and floating InSAR. *Earth and Planetary Science Letters*, *576*, 117241. https://doi.org/10.1016/j.epsl.2021.117241

Yamazaki, Y., Cheung, K. F., & Kowalik, Z. (2011). Depth-integrated, non-hydrostatic model with grid nesting for tsunami generation, propagation, and run-up. *International Journal for Numerical Methods in Fluids*, *67*(12), 2081–2107. https://doi.org/10.1002/fld.2485

Yamazaki, Y., Cheung, K. F., & Lay, T. (2013). Modeling of the 2011 Tohoku near-field tsunami from finite-fault inversion of seismic waves. *Bulletin of the Seismological Society of America*, *103*, 1444–1455. https://doi.org/10.1785/0120120103

Yamazaki, Y., Cheung, K. F., & Lay, T. (2018). A self-consistent fault slip model for the 2011 Tohoku earthquake and tsunami. *Journal of Geophysical Research: Solid Earth*, *123*, 1435–1458. https://doi.org/10.1002/2017JB014749

Yamazaki, Y., Kowalik, Z., & Cheung, K. F. (2009). Depth-integrated, non-hydrostatic model for wave breaking and run-up. *International Journal for Numerical Methods in Fluids*, *61*(5), 473–497. https://doi.org/10.1002/fld.1952

Yamazaki, Y., Lay, T., Cheung, K. F., Yue, H., & Kanamori, H. (2011). Modeling near-field tsunami observations to improve finite-fault slip models for the 11 March 2011 Tohoku earthquake. *Geophysical Research Letters*, *38*, L00G15. https://doi.org/10.1029/2011GL049130

Ye, L., Kanamori, H., Avouac, J.-P., Li, L., Cheung, K. F., & Lay, T. (2016). The 16 April 2016, M_W 7.8 (M_S 7.5) Ecuador earthquake: A quasi-repeat of the 1942 M_S 7.5 earthquake and partial re-rupture of the 1906 M_S 8.6 Colombia-Ecuador earthquake. *Earth and Planetary Science Letters*, *454*, 248–258. https://doi.org/10.1016/j.epsl.2016.09.006

Ye, L., Lay, T., & Kanamori, H. (2020). Anomalously low aftershock productivity of the 2019 M_W 8.0 energetic intermediate-depth faulting beneath Peru. *Earth and Planetary Science Letters*, *540*, 116528.

Ye, L., Lay, T., Kanamori, H., & Rivera, L. (2016). Rupture characteristics of major and great ($M_W \geq 7.0$) megathrust earthquakes from 1990 to 2015: 1. Source parameter scaling relationships. *Journal of Geophysical Research: Solid Earth*, *121*, 826–844. https://doi.org/10.1002/2015JB012426

Ye, L., Lay, T., Kanamori, H., Yamazaki, Y., & Cheung, K. F. (2021). The 22 July 2020 M_W 7.8 Shumagin seismic gap earthquake: Partial rupture of a weakly coupled megathrust. *Earth and Planetary Science Letters*, *562*, 116879. https://doi.org/10.1016/j.epsl.2021.116879

Yokota, Y., Koketsu, K., Fujii, Y., Satake, K., Sakai, S., Shinohara, M., & Kanazawa, T. (2011). Joint inversion of strong motion, teleseismic, geodetic, and tsunami datasets for the rupture process of the 2011 Tohoku earthquake. *Geophysical Research Letters*, *38*, L00G21. https://doi.org/10.1029/2011GL050098

Yue, H., Lay, T., Rivera, L., Bai, Y., Yamazaki, Y., Cheung, K. F., et al. (2014). Rupture process of the 2010 M_W 7.8 Mentawai tsunami earthquake from joint inversion of near-field hr-GPS and teleseismic body wave recordings constrained by tsunami observations. *Journal of Geophysical Research: Solid Earth*, *119*, 5574–5593. https://doi.org/10.1002/2014JB011082

AGU PUBLICATIONS

Journal of Geophysical Research: Solid Earth

Supporting Information for

Rupture Model for the 29 July 2021 M_W 8.2 Chignik, Alaska Earthquake Constrained by Seismic, Geodetic, and Tsunami Observations

Lingling Ye[1], Yefei Bai[2], Daojun Si[1], Thorne Lay[3], Kwok Fai Cheung[4], and Hiroo Kanamori[5]

[1]Department of Earth and Space Sciences, Southern University of Science and Technology, Shenzhen, Guangdong, 518055, China.

[2]Ocean College, Zhejiang University, Zhoushan, Zhejiang, 316021, China.

[3]Department of Earth and Planetary Sciences, University of California Santa Cruz, Santa Cruz, California, 95064, USA.

[4]Department of Ocean and Resources Engineering, University of Hawaii at Manoa, Honolulu, HI, 96822, USA.

[5]Seismological Laboratory, California Institute of Technology, Pasadena, California, 91125, USA.

Contents of this file

Introduction

This supplement includes a table listing observed and predicted GNSS offsets (Table S1), and figures that show the geometry of the preferred model relative to seismicity and plate boundary interface models (Figure S1), inversions for two additional models with tsunami predictions (Figures S2 and S3), and sensitivity to smoothing in the inversion of seismic and geodetic data (Figure S4). It also provides captions for two animations (Movies S1 and S2), which are provided as separate files.

Table S1 GNSS coseismic offsets and model predictions from our preferred model (Figure 2)

Site	Lon (˚E)	Lat (˚N)	East (cm)	North (cm)	Up (cm)	E_Model (cm)	N_Model (cm)	Up_Model (cm)
AB13	-158.5038	56.3073	25.620	-37.088	-6.928	23.034	-34.088	-12.458
AC13	-155.6224	55.8219	24.323	-15.454	6.622	22.898	-14.183	7.638
AC21	-159.1277	55.9211	31.664	-26.459	-7.595	29.374	-22.765	-12.717
AC40	-158.6186	56.9304	9.985	-17.796	-0.140	8.170	-15.303	-2.503
AC41	-160.4073	55.9087	8.868	-4.571	-0.053	8.877	-4.248	-1.878
AB07	-160.4768	55.3493	6.461	-2.414	-0.766	4.676	-0.992	-1.676
AC28	-160.0492	55.0785	2.890	-1.060	-1.125	2.228	-0.508	-1.791
AC12	-159.5896	54.8310	-1.590	-2.069	-0.899	-2.578	-1.897	-0.841
AC52	-157.5742	57.5673	2.255	-8.867	0.677	1.740	-7.972	-0.871
AC25	-162.3141	55.0890	1.494	-0.692	0.026	1.164	-0.290	-0.489

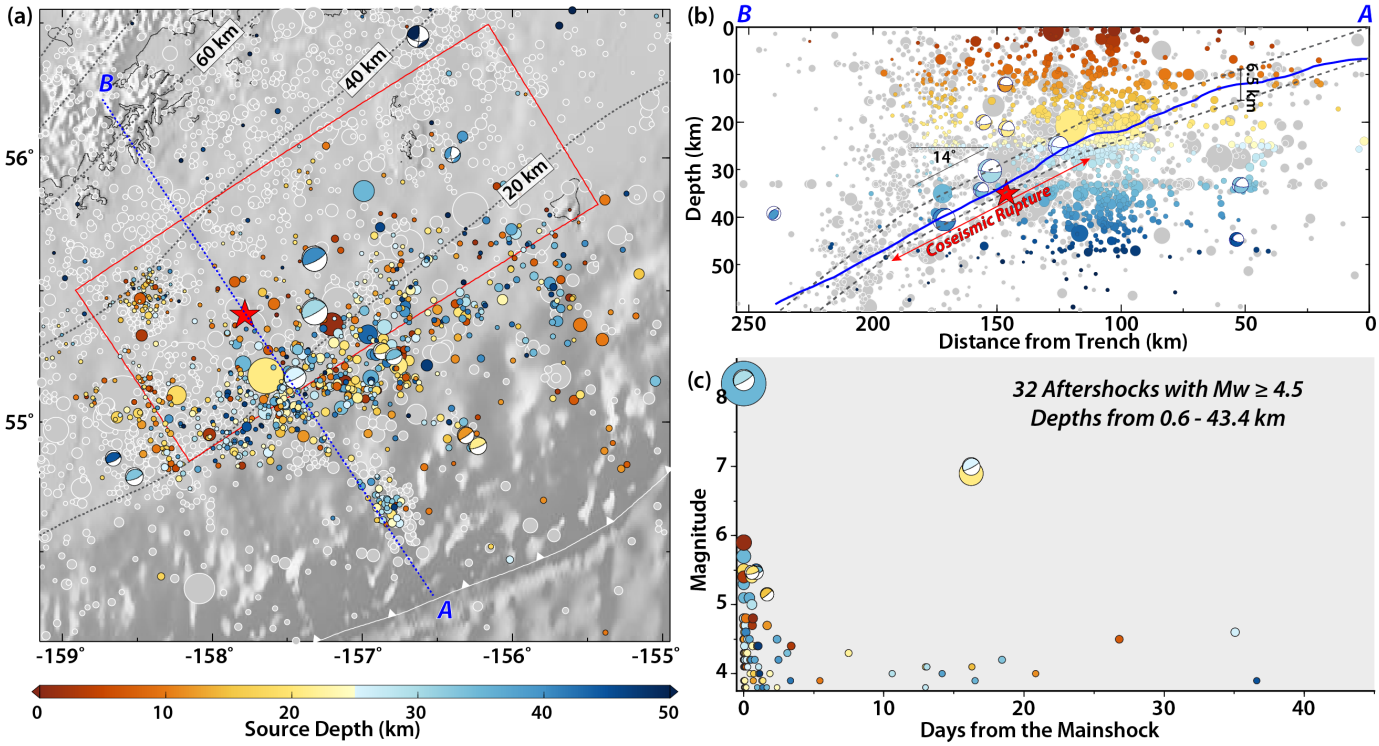

Figure S1. Slab Geometry and aftershock productivity for the 2021 Chignik, Alaska earthquake. (a) Regional seismicity from the USGS-NEIC catalog with M>2.5 within 4 months after the 2021 M_W 8.2 event (circles with radius scaled by magnitude), along with historical events from 1900 to 2021 shown by gray circles. All gCMT focal mechanisms for aftershocks are color-coded by the source depth. The red rectangle indicates the fault geometry for our preferred slip model (Figure 2), along with the epicenter (red star) used in the inversion. Blue dashed line shows the projection direction of the vertical profile in (b). (b) The vertical profile of seismicity and main slip depth range projected along transect A-B direction. The blue curve shows the plate interface depth from the ALEUT multichannel seismic survey (ALEUT 3; adapted from Figure 3.8.2 in the Ph.D. thesis of Harold Kuehn: https://dalspace.library.dal.ca/handle/10222/75145). The top dashed curve shows the slab geometry from Slab2 (Hayes et al., 2018) which is also shifted by 6.5 km deeper (lower dashed curve) to match the hypocenter depth of the 2021 mainshock. The red two-headed arrow indicates the depth range of our preferred slip model with a dip angle of 14°. (c) The time sequence of aftershocks with $m_b \geq$ 4.5 in a 45-day window after the main event within a radius of 500 km from the USGS-NEIC epicenter.

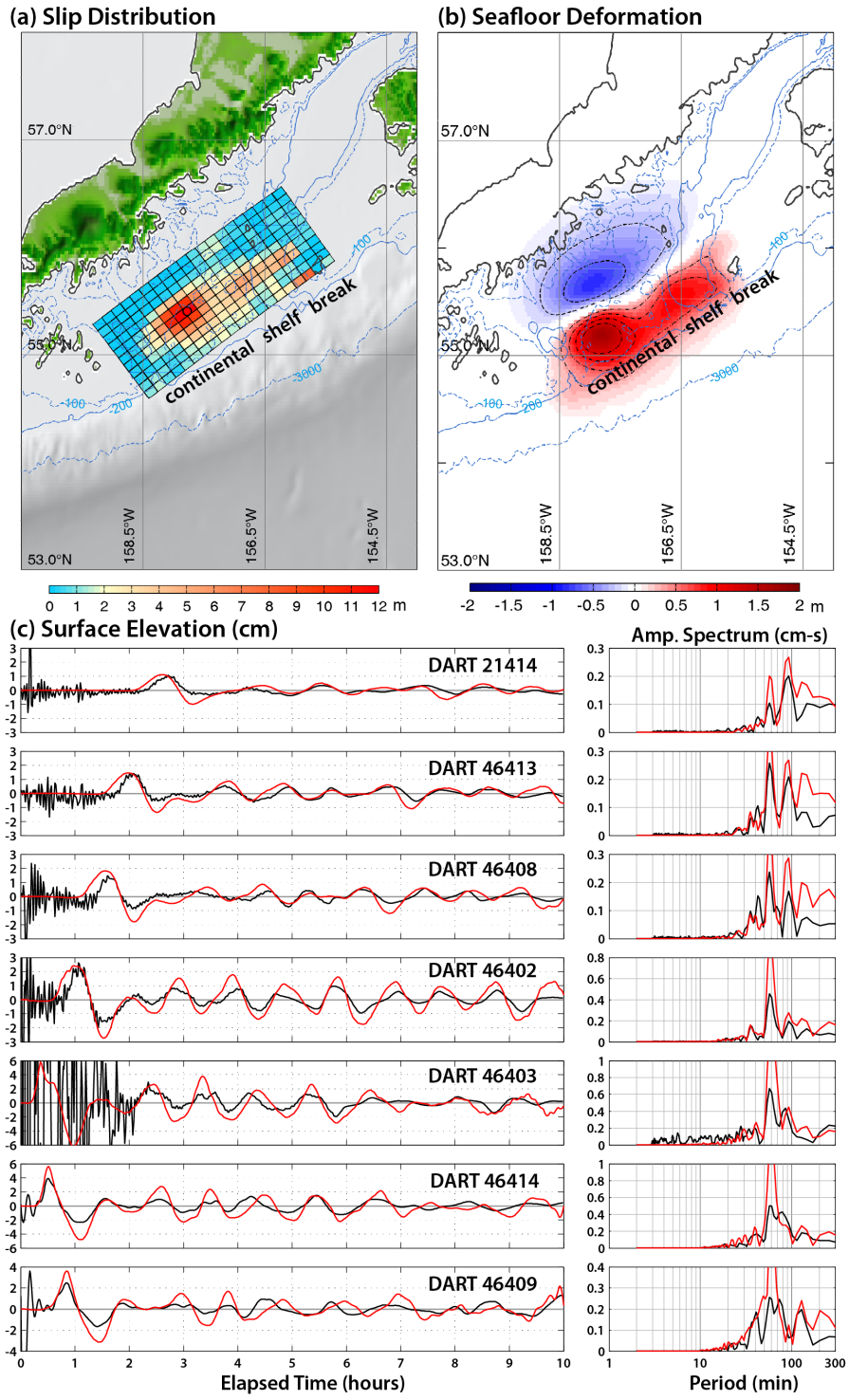

Figure S2. Seafloor deformation and tsunami prediction from the inverted slip model on the fault plane with strike of 233.2° and dip of 15.2° from our Wphase solution. (a) The inverted slip distribution with the epicenter from USGS-NEIC (Lat 55.364°N, Lon 157.888°W). (b) The calculated seafloor deformation for a half space (Okada, 1985). (c) Comparison of observed (black) and computed (red) sea surface elevation time series and spectra for DART stations. The predicated tsunami arrivals are too early for DART stations to the west (21414, 45413, 46408 and 46402), and the tsunami amplitudes are overpredicted for DART stations to the south (46403) and to the east (46414 and 46409).

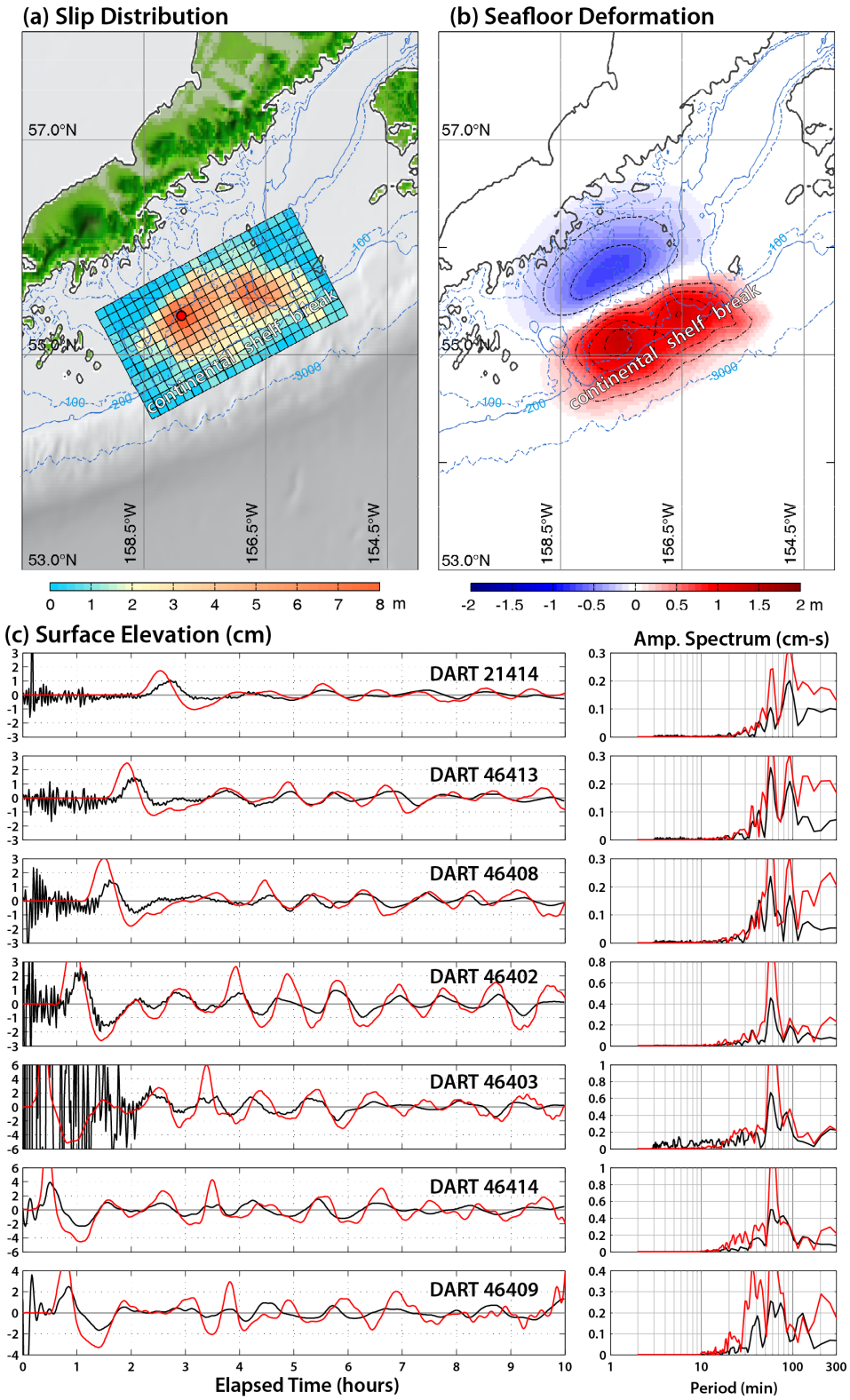

Figure S3. Seafloor deformation and tsunami prediction from the slip model by Liu et al. (2022). Layouts are the same as in Figure S2. Note that the predicted tsunamis are too early, and the amplitudes are overpredicted for all stations due to having a large amount of slip near the continental shelf break, with seafloor uplift extending out onto the continental slope.

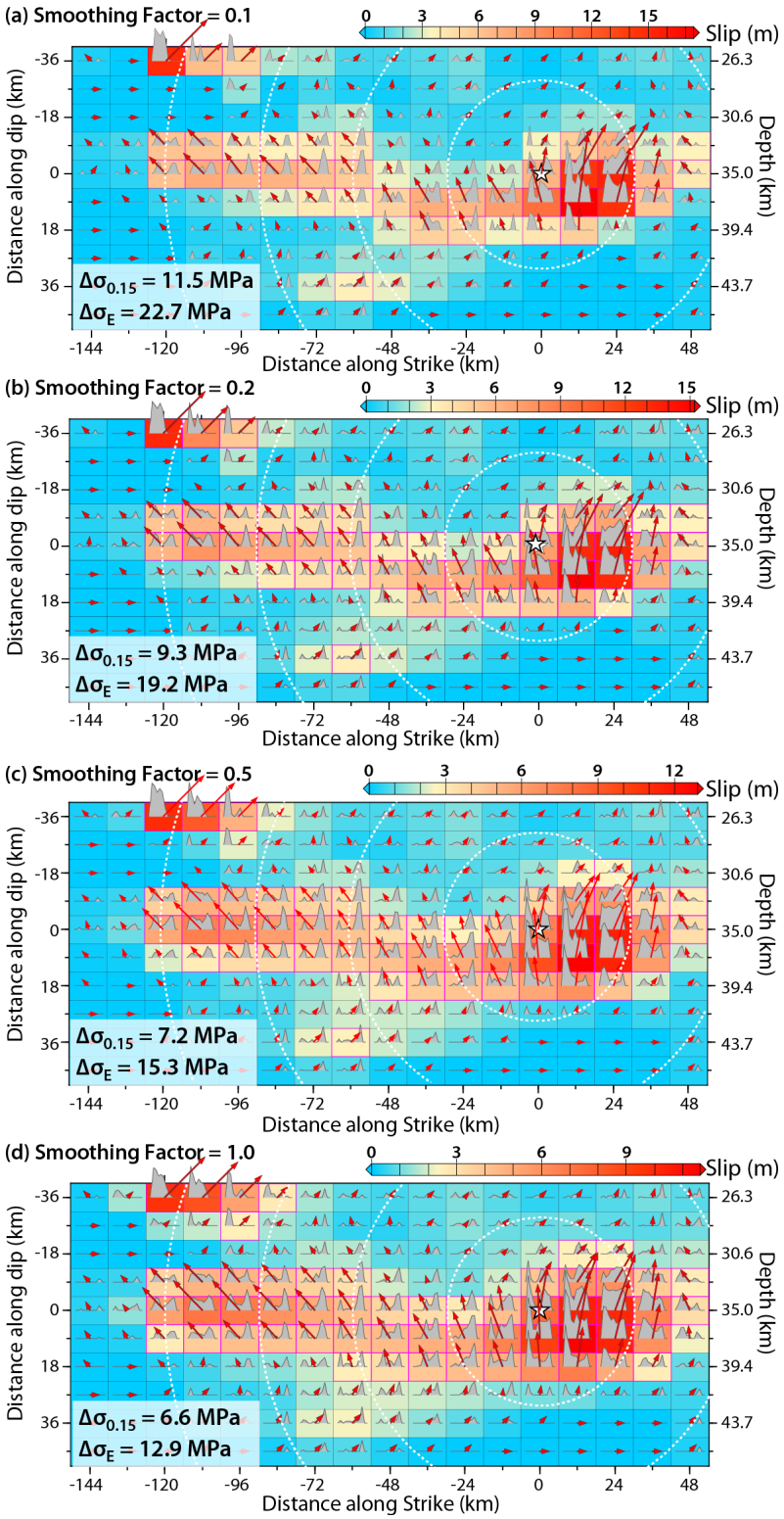

Figure S4. Comparisons of slip models having the same model setup and total seismic moment, but with different smoothing factors of (a) 0.1, (b) 0.2, (c) 0.5, and (d) 1.0. There is little difference in slip distribution, but the peak slip and stress drop decrease as the smoothing factor increases. The panel (c) is our preferred slip model. There is very little variation in the predictions of seismic, geodetic and tsunami data from these models, and all fit the data well.

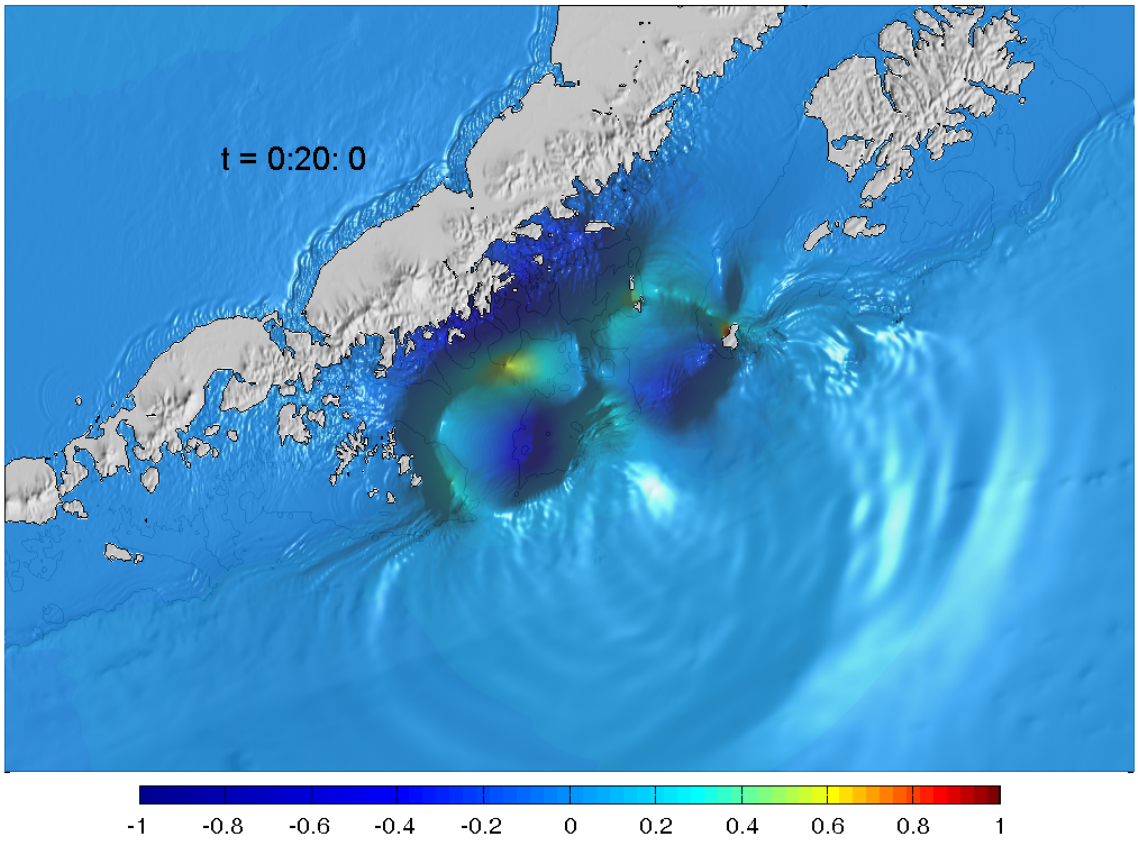

Movie S1. Movie for tsunami sea surface near the source region for our preferred model in Figure 2.

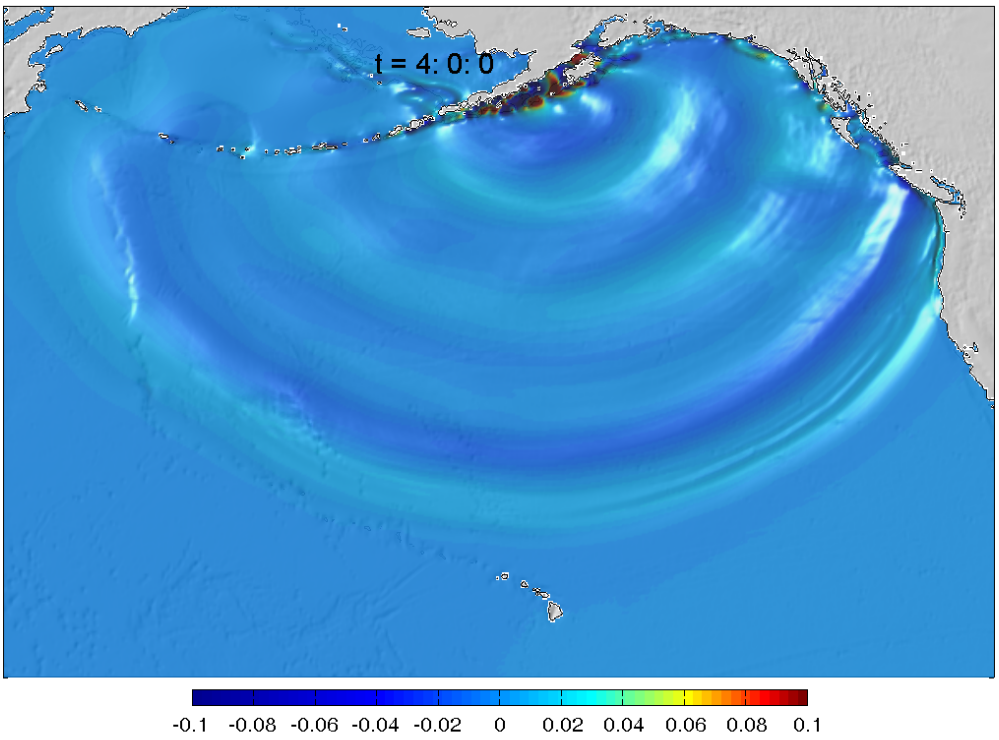

Movie S2. Movie for tsunami sea surface across the North Pacific for our preferred model in Figure 2.